

# A Deep-Learning Hybrid-Predictive-Modeling (HPM) Approach for Estimating Evapotranspiration and Ecosystem Respiration

Jiancong Chen<sup>1</sup>, Baptiste Dafflon<sup>2</sup>, Anh Phuong Tran<sup>2,3</sup>, Nicola Falco<sup>2</sup>, and Susan S. Hubbard<sup>2</sup>

<sup>1</sup>Department of Civil and Environmental Engineering, University of California, Berkeley, CA, USA, <sup>2</sup>Earth and Environmental Sciences Area, Lawrence Berkeley National Laboratory, Berkeley, CA, USA, <sup>3</sup>Department of Water Resources Engineering and Technology, Water Resources Institute, 8, Phao Dai Lang, Dong Da, Hanoi, Vietnam

**Abstract:** Gradual changes in meteorological forcings (such as temperature and precipitation) are reshaping vulnerable ecosystems, leading to uncertain effects on ecosystem dynamics, including water and carbon fluxes. Estimating evapotranspiration (ET) and ecosystem respiration ( $R_{eco}$ ) is essential for analyzing the effect of climate change on ecosystem behavior. To obtain a better understanding of these processes, we need to improve our  $R_{eco}$ . However, accurate estimation of water and carbon fluxes over space and time, which is difficult within ecosystems that often have only sparse ET and  $R_{eco}$ , still remains challenging at sparsely monitored watersheds where data and field instrumentation are limited. In this study, we developed a hybrid predictive modeling approach (HPM) that integrates eddy covariance measurements, physically-based model simulation results, meteorological forcings, and remote sensing datasets to estimate evapotranspiration (ET) and ecosystem respiration ( $R_{eco}$ ) in high space-time resolution. HPM relies on a deep learning algorithm with long short-term memory (LSTM) as well as direct measurements or outputs from physically-based models, and requires only air temperature, precipitation, radiation, normalized difference vegetation index (NDVI) and soil temperature (when available) as input variables. We tested and validated HPM estimation results at sites within various sites. We particularly focus on testing HPM in mountainous regions, given their importance for water resources, their vulnerability to climate change, and the recognized difficulties in estimating ET and  $R_{eco}$  in such regions. We benchmarked daily scale estimates of ET and  $R_{eco}$  obtained from the HPM method against measurements made at FLUXNET stations and outputs from the Community Land Model (CLM) at in different climate regions and developed four use cases to demonstrate the applicability and variability of HPM at various FLUXNET sites and Rocky Mountain SNOTEL stations. At the mountainous sites in Western North America. To test the limitations and performance of HPMs in mountainous watersheds, an expanded use case focused on the East River Watershed site in the Upper Colorado River Basin, we explored how ET and  $R_{eco}$  dynamics estimated from the new HPM approach vary with different vegetation and meteorological forcings in USA. The results of this study indicate that HPM is capable of identifying complicated interactions among meteorological forcings, ET, and  $R_{eco}$  variables, as well as providing reliable estimation of ET and  $R_{eco}$  across relevant spatiotemporal scales, even in challenging mountainous systems. With HPM estimation of ET and  $R_{eco}$  at the East River Watershed, we identified that HPM ET models are sensitive to temperature and radiation inputs whereas NDVI, temperature and radiation all have crucial influences over  $R_{eco}$  dynamics. In general, our study demonstrated that the HPM approach can circumvent the typical lack of spatiotemporally dense data needed. The study documents that HPM increases our capability to estimate ET and  $R_{eco}$  over space and time, as well as the parametric and structural uncertainty inherent in mechanistic models. While the

38 current limitations of the HPM approach are driven by the temporal and spatial resolution of available datasets (such  
39 as meteorological forcing and NDVI data), ongoing advances are expected to further improve accuracy and resolution  
40 of ET and  $R_{eco}$  estimation using HPM  $R_{eco}$  and enhances process understanding at sparsely monitored watersheds.

#### 41 1. Introduction:

42 ~~Evapotranspiration~~Climate change has a profound influence on global and regional energy, water and carbon  
43 ~~cycling, including evapotranspiration~~ (ET) and ecosystem respiration ( $R_{eco}$ ) are key components of ecosystem water  
44 ~~and carbon cycles ( $R_{eco}$ ).~~ ET is an important link between the water and energy cycles: dynamic changes in ET can  
45 affect precipitation, soil moisture, and surface temperature, leading to uncertain feedbacks in the environment (Jung  
46 et al., 2010; Seneviratne et al., 2006; Teuling et al., 2013). Thus, quantifying ET is particularly essential for improving  
47 our understanding of water and energy interactions ~~and as well as~~ watershed ~~response~~ responses to abrupt ~~disturbances~~  
48 and gradual ~~climate~~ changes ~~in climate~~, which is critical for water resources management, agriculture, and other  
49 societal benefits (Anderson et al., 2012; Jung et al., 2010; Rungee et al., 2019; Viviroli et al., 2007; Viviroli and  
50 Weingartner, 2008).  ~~$R_{eco}$~~   $R_{eco}$ , which represents ~~the sum of autotrophic total~~ respiration ~~and respiration by~~  
51 ~~heterotrophic microorganisms~~ in a specific ecosystem, plays a vital role in the response of terrestrial ecosystem to  
52 global change (Jung et al., 2017; Reichstein et al., 2005; Xu et al., 2004). ~~As long term exchanges in  $R_{eco}$  have pivotal~~  
53 ~~influences over the climate system~~ While increases in  $R_{eco}$  may contribute to accelerating global warming through  
54 ~~positive feedbacks to the atmosphere~~ (Cox et al., 2000; Gao et al., 2017; IPCC, 2019; Suleau et al., 2011), ~~approaches~~  
55 ~~are needed to estimate~~ ~~estimating~~ and ~~monitor~~  $R_{eco}$  ~~monitoring~~  $R_{eco}$  over relevant spatiotemporal scales: ~~is challenging~~.  
56 As described below, there are many different strategies for measuring and estimating ET and  ~~$R_{eco}$~~   $R_{eco}$ , each of which  
57 has advantages and limitations. ~~The motivation for this~~ This study is ~~motivated by~~ the recognition that current methods  
58 cannot provide ET and  ~~$R_{eco}$~~   $R_{eco}$  at space and time scales (e.g., daily) needed to improve prediction of changing  
59 terrestrial system behavior, particularly in challenging mountainous watersheds.

60 Several ground-based approaches have been used to provide *in situ* estimates or measurements of ET and  
61  ~~$R_{eco}$~~   $R_{eco}$ . Ground-based flux chambers ~~capture and~~ measure trace gases emitted from the land surface, which can be  
62 used to estimate ET and  ~~$R_{eco}$~~   $R_{eco}$  (Livingston and Hutchinson, 1995; Pumpanen et al., 2004). ~~However, the~~  
63 ~~microclimate of the environment is affected by the chamber, and the laborious acquisition process and small chamber~~  
64 ~~size typically lead to information with coarse spatiotemporal resolution (Baldochi, 2014).~~ The eddy covariance  
65 method uses a tower with installed instruments to autonomously measure fluxes of trace gases between ecosystem and  
66 atmosphere (Baldochi, 2014; Wilson et al., 2001). ~~The covariance between the vertical velocity and mixing ratios of~~  
67 ~~the target scalar is computed to obtain the fluxes of carbon, water vapor, and other trace gases emitted from the land~~  
68 ~~surface.~~ ET is then calculated from the latent heat flux, and  ~~$R_{eco}$~~   $R_{eco}$  is calculated from the net carbon fluxes using  
69 night-time or daytime partitioning approaches (van Gorsel et al., 2009; Lasslop et al., 2010; Reichstein et al., 2005).  
70 The spatial footprint of obtained ~~eddy covariance~~ fluxes is on the order of hundreds of meters, and the temporal  
71 resolution of the measurements ~~range~~ ranges from hours to decades (Wilson et al., 2001). ~~Such~~ Tower-based ~~in-situ~~  
72 measurements of fluxes have been integrated into the global AmeriFlux (<http://ameriflux.lbl.gov/>) and FLUXNET  
73 (<https://FLUXNET.fluxdata.org/>) networks, ~~where such data have greatly benefited process investigations and model~~  
74 ~~development undertaken by a wide scientific community.~~ However, given the cost, effort, and power required to install

Formatted: Subscript

Formatted: Font: Not Italic

Formatted: Font: Not Italic

75 and maintain a flux tower, eddy covariance towers are typically sparse relative to the scale of study sites used to  
76 address ecosystem questions. Additionally, the location of a flux tower within a watershed greatly influences  
77 measurement representativeness. For example, for logistical reasons, eddy covariance towers are usually  
78 installed at valley bottoms of mountainous watersheds (Strachan et al., 2016). However, microclimate caused by  
79 complex mountainous terrains (e.g., slope, aspect and elevation) can have different radiation inputs and moisture  
80 dynamics compared to flat areas where flux towers are mostly installed. Flux measurements from eddy covariance  
81 towers provide a representation of major driver and controls on ET and  $R_{ECO}$  in an ecoregion while meteorological  
82 forcing variability needs to be accounted to possibly represent various aspects introduced by complex terrain. Thus,  
83 though measurements from a single flux tower may not capture heterogeneity in ET and  $R_{ECO}$  due to complex terrain,  
84 theyData from flux towers should also be used carefully as flux footprints may vary significantly across sites and  
85 through time depending on site-specific information, turbulent states of the atmosphere and underlying surface  
86 characteristics (Chu et al., 2021). Given the cost and efforts required to install and maintain a flux tower, eddy  
87 covariance towers are typically sparse and may not capture complex fluxes at sites with complex terrains, such as  
88 montane environments. Though measurements from a single flux tower may not capture heterogeneity in ET and  $R_{ECO}$   
89 due to complex terrains, they can support the development of statistical or physical-based models integrated with other  
90 types of data to provide ET and  $R_{ECO}$  estimation in high resolution over space and time as we describe herein.

91 Physically-based numerical models, which numerically represent land-surface energy and water balance,  
92 have also been used to estimate ET and  $R_{ECO}$  (Tran et al., 2019; Williams et al., 2009). These physically based  
93 models solve physical equations to simulate the exchanges of energy, heat, water and carbon across atmosphere-  
94 canopy-soil compartments. Examples include, such as the Community Land Model (CLM, Oleson et al., 2013).  
95 Performance of these models depends on the accuracy of inputs and parameters, such as soil type and leaf area  
96 index, which can be difficult to obtain at a sufficiently high spatiotemporal resolution. The lack of measurements to  
97 infer parameters needed for models often leads to large discrepancies between model-based and flux-tower-based ET  
98 and  $R_{ECO}$  estimates. Conceptual model uncertainty inherent in mechanistic models can also lead to ET and  $R_{ECO}$   
99 estimation uncertainty and errors. For example, Keenan et al. (2019) suggested that current terrestrial carbon cycle  
100 models neglect inhibition of leaf respiration that occurs during daytime, which can result in a bias of up to 25 %.  
101 Chang et al. (2018) used virtual experiments with 3-D terrestrial integrated modeling system to investigate why a  
102 lower ratio of transpiration to ET is always produced by large scale land surface models. Their study suggested  
103 heterogeneous fluxes caused by uneven hydraulic distribution due to complex terrain are not always considered in  
104 process-based models. These conceptual uncertainties, in addition to data sparseness and data uncertainty, further limit  
105 the applicability of physically based models to estimate ET and  $R_{ECO}$  at high spatiotemporal scales. Semi-analytical  
106 formulations based on combinations of meteorological and empirical parameters provide a reference condition for the  
107 water and energy balance. Examples used to estimate potential ET includesuggested that process-based models may  
108 not represent transpiration accurately due to challenges in simulating the uneven hydraulic distribution caused by  
109 complex terrain. Semi-analytical formulations are also commonly used to estimate ET, including the Budyko  
110 framework and its extensions (Budyko, 1961; Greve et al., 2015; Zhang et al., 2008); the Penman-Monteith's equation  
111 (Allen et al., 1998), and the Priestley-Taylor equation (Priestley and Taylor, 1972)(Priestley and Taylor, 1972). Actual

Formatted: Subscript

112 ET can then be approximated by multiplying a coefficient associated with water deficit (De Bruin, 1983; Williams &  
113 Albertson, 2004). However, even with these empirical formulations many attributes are still difficult to obtain globally  
114 at high temporal scales, such as water vapor deficit, leaf area index, and aerodynamic conductance of different  
115 plants. However, these conceptual uncertainties, in addition to data sparseness and data uncertainty, still limit the  
116 applicability of these approaches.

117 Remote sensing products, such as Landsat imagery (Irons et al., 2012), Sentinel-2 (Main-Knorn et al., 2017)  
118 and the moderate-resolution imaging spectroradiometer (MODIS, NASA, 2008), have also been integrated to estimate  
119 ET and  $R_{ECO}$  with empirical, statistical, or semi-physical relations  $R_{ECO}$  (Abatzoglou et al., 2014; Daggars et al., 2018;  
120 Mohanty et al., 2017; Paca et al., 2019). Due to the high spatial coverage of remote sensing products, global-scale  
121 estimates of ET and  $R_{ECO}$  have become feasible. For example, Ryu et al. (2011) proposed the 'Breathing Earth System  
122 Simulator' approach, which integrates mechanistic models and MODIS data to quantify ET and GPP with  
123 a spatial resolution of 1-5 km and a temporal resolution of 8 days. Ai et al. (2018) extracted enhanced vegetation index,  
124 fraction of absorbed photosynthetically active radiation, and leaf area index indices from the MODIS dataset—and  
125 used the rate-temperature curve and strong correlations between terrestrial carbon exchange and air temperature to  
126 estimate  $R_{ECO}$  at 1 km spatial resolution and 8-day temporal resolution. Ma et al. (2018) developed a data fusion  
127 scheme that fused Landsat-like-scale datasets and MODIS data to estimate ET and irrigation water efficiency at a  
128 spatial scale of ~100 meters. However, even though remote sensing data cover large areas of the earth surface, they  
129 typically do not provide information over both high spatial and temporal resolution, and are also data quality is subject  
130 to cloudy conditions. For example, Landsat has average return periods of 16 days with a spatial resolution of 30  
131 m (visible and near-infrared), whereas MODIS has 1-2 days temporal resolution with a 250 m or 1 km spatial  
132 resolution depending on the sensors. These resolutions are typically too coarse to enable exploration of how aspects  
133 such as plant phenology, snowmelt, and rainfall impact integrated ecosystem influence water and energy dynamics of  
134 an ecosystem.

135 Combining machine-learning models with remote sensing products and meteorological inputs offers another  
136 option for large-scale estimation of ET and  $R_{ECO}$ . Remotely sensed data can be good proxies for plant productivity  
137 and can be easily implemented into machine-learning models for ET and  $R_{ECO}$  estimation, such as for an enhanced  
138 vegetation index, land surface water index and normalized differences vegetation index (NDVI) (Gao et al., 2015;  
139 Jägermeyr et al., 2014; Migliavacca et al., 2015). Li and Xiao (2019) developed a data-driven model to estimate gross  
140 primary production at a spatial and temporal resolution of 0.05° and 8 days, respectively, using MODIS and  
141 meteorological reanalysis data. Berryman et al. (2018) demonstrated the value of a Random Forest model to predict  
142 growing season soil respiration from subalpine forests in the Southern Rocky Mountains ecoregion. Jung et al. (2009)  
143 developed a model tree ensemble approach to upscale FLUXNET data, where they successfully estimated ET and  
144 GPP. Other methods have used support vector machines, artificial neural networks, random forest, and piecewise  
145 regression (Bodesheim et al., 2018; Metzger et al., 2013; Xiao et al., 2014; Xu et al., 2018). These models were trained  
146 with ground-measured flux observations and other variables, and then applied to estimate ET over continental or  
147 global scales with remote sensing and meteorological inputs. Some of the most important inputs include the enhanced

148 vegetation index, aridity index, air temperature, and precipitation. ~~However, the~~The spatiotemporal resolution of these  
149 approaches is constrained by the resolution of remote sensing products and meteorological inputs. Additionally,  
150 parameters such as leaf area index, cloudiness, and the vegetation types required by those models may not be available  
151 at the required resolution, accuracy or location. For example, in systems that have significant elevation gradients,  
152 errors may result occur when valley-based FLUXNET data are used for training and then applied to hillslope or ridge  
153 ET and  $R_{ETCO}R_{eco}$  estimation.

154 Development of hybrid models that link direct measurements and/or ~~interpretable~~mechanistic models with  
155 data-driven methods can benefit ET and  $R_{ETCO}R_{eco}$  estimation (Reichstein et al., 2019). While remote sensing data that  
156 cover large regions provide promise for informing models, quantitative interpretation of these data needed for input  
157 into mechanistic models is still challenging (Reichstein et al., 2019). Physically-based models can provide estimates  
158 of ET and  $R_{ETCO}R_{eco}$ , but the estimate error can be high, owing to parametric, structural, and conceptual uncertainties  
159 as described above. Hybrid data-driven frameworks are ~~potentially~~advantageous because they enable the integration  
160 of remote sensing datasets, meteorological forcings, and mechanistic model outputs of ET and  $R_{ETCO}R_{eco}$  into one  
161 model. Machine-learning approaches ~~are can~~ then ~~be~~ applied to extract the spatiotemporal patterns for ET and  $R_{ETCO}R_{eco}$   
162 prediction. ~~Hybrid models can utilize the high spatial coverage~~The integration of ~~remote sensing multi-model and~~  
163 ~~multi-data (e.g., 30 m of Landsat) and high temporal resolution of direct measurement from flux towers or simulation~~  
164 ~~results from mechanistic models (e.g., daily or hourly scales), thus providing alternative approaches for next stage,~~  
165 ~~more accurate estimation of~~can increase our modeling capability to estimate ET and  $R_{ETCO}$  at greater spatial $R_{eco}$  and  
166 ~~finer temporal scales—and enhance~~enhance our process understanding of ecosystem water and carbon cycling under  
167 climate change.

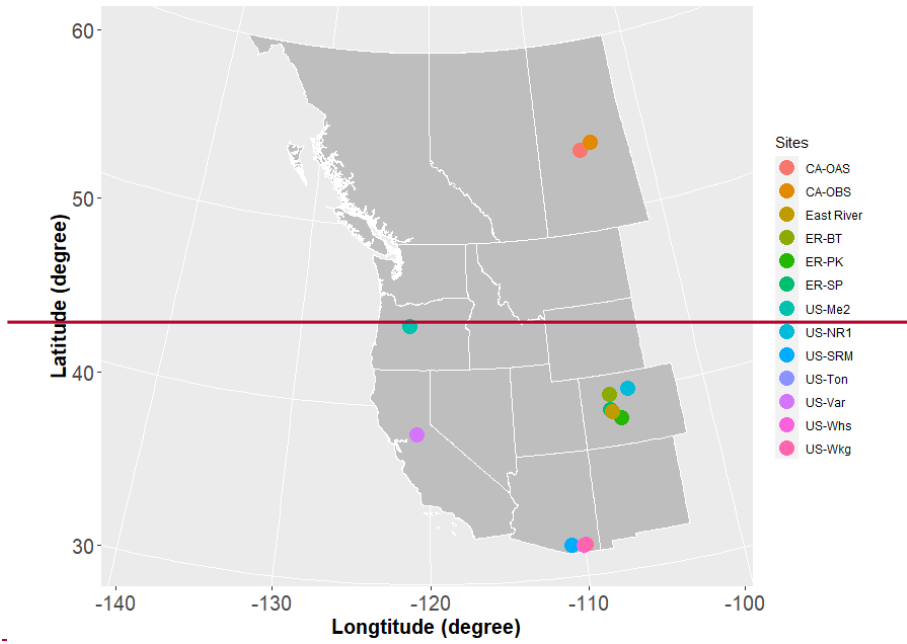
168 In this study, we developed a hybrid predictive modeling approach (HPM) to ~~better~~estimate daily ET and  
169  $R_{ECO}$  with easily acquired meteorological data (i.e., air temperature, precipitation and radiation) and remote sensing  
170 products (i.e., NDVI). HPM is hybrid as it can ~~use deep learning models to flexibly~~ integrate direct measurements from  
171 flux towers and/or physically-based model results (e.g., CLM) ~~with and utilize deep learning long-short term memory~~  
172 ~~recurrent neural network (LSTM) to establish statistical relationships among fluxes,~~ meteorological and remote  
173 sensing inputs ~~to capture.~~ Once developed, the ~~complex physical interactions within the watershed ecosystem. After~~  
174 ~~development, we validated corresponding~~ HPM performance with the FLUXNET dataset and benchmarked the CLM  
175 ~~model at select sites. We then~~can be used the HPM foras a modeling tool to estimate ET and  $R_{ETCO}$  estimation at the  
176 ~~mountainous East River Watershed in Colorado, USA~~ $R_{eco}$  over space and investigated how ETtime. We developed  
177 ~~four use cases to demonstrate the applicability of HPM based on site-specific data and~~  $R_{ETCO}$  dynamics varies within  
178 ~~the East River Watershed.~~

179 model availability. The remainder of this paper is organized as follows. Section 2 mainly describes the sites  
180 considered in this study and how data were acquired and processed. Section 3 presents the methodology of the HPM  
181 approach, followed by the results of various use cases presented in Section 4. Discussion and conclusion are provided  
182 in Sections 5 and 6, respectively.

Formatted: Subscript

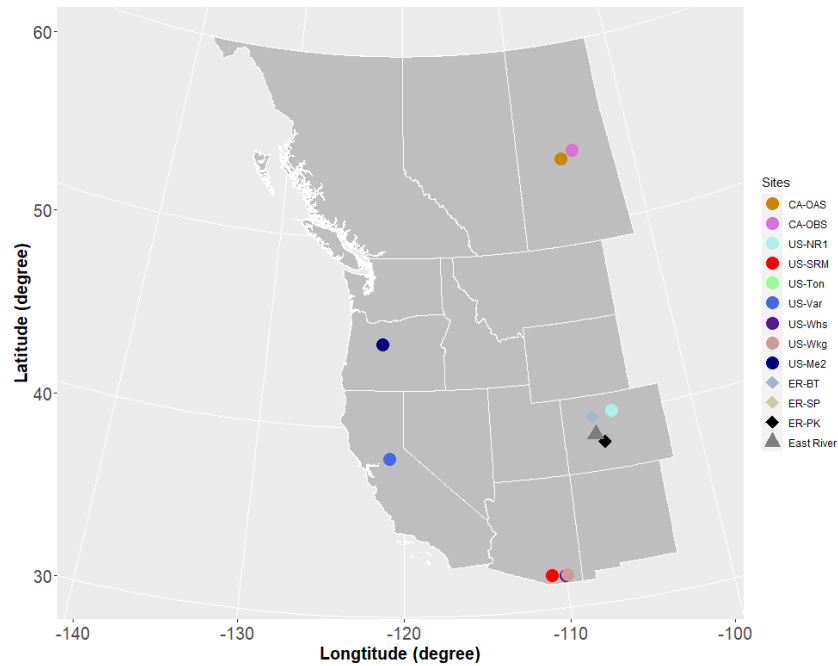








217



218

219 **Figure 1. Location of sites considered in this study. Note: US-Ton and US-Var; US-Whs and US-Wkg are at the same**  
 220 **locations, closed to each other.** East River Watershed is located next to ER-BT. The white lines delineate Western US states  
 221 **and Canadian provinces. Circles represent FLUXNET sites, diamonds represent SNOTEL sites and triangle represents the**  
 222 **East River Watershed.**

223 **2.3 East River Watershed Characteristics and Previous Analyses**

224 Data from the East River Watershed were used to explore how ET and  $R_{eco}^{Reco}$  dynamics estimated from  
 225 the developed HPM vary with different vegetation and meteorological forcings. The East River Watershed is located  
 226 northeast of the town of Crested Butte, Colorado. This watershed has an average elevation of 3266 m, with significant  
 227 gradients in topography, hydrology, geomorphology, vegetation, and weather. ~~The watershed has a mean annual~~  
 228 ~~temperature around 0°C, with an average of 1200 mm yr<sup>-1</sup>~~The mean annual air temperature in the East River is  
 229 ~~~2.4°C, with average daily air temperatures of -7.6°C and 13.4°C in December and July respectively (Kakalia et al.,~~  
 230 ~~2020) and an average of 1200 mm yr<sup>-1</sup>~~ total precipitation (Hubbard et al., 2018). Consisting of montane, subalpine,  
 231 and alpine life zones, each with distinctive vegetation biodiversity, the East River Watershed is a testbed for the US  
 232 Department of Energy Watershed Function Scientific Focus Area Project, led by the Lawrence Berkeley National  
 233 Laboratory (Hubbard et al., 2018). The project has acquired a range of datasets, including hydrological,  
 234 biogeochemical, remote sensing, and geophysical datasets.

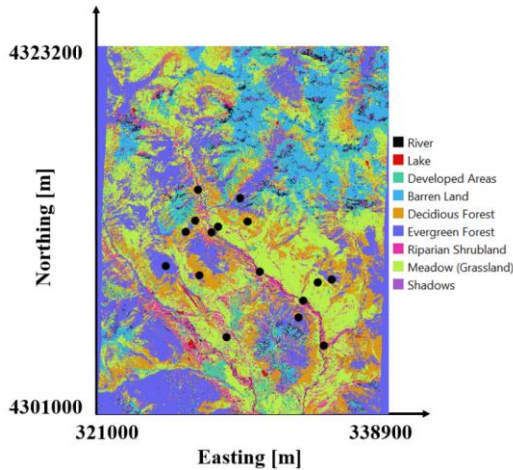
Formatted: Subscript

235 Recently completed studies at the East River Watershed were used in this study to inform HPM and to assess  
 236 the results. For example, physically-model-based estimations of ET at this site (Tran et al., 2019) were used herein for  
 237 HPM development and validation. Falco et al. (2019) used machine-learning-based remote sensing methods to  
 238 characterize the spatial distribution of vegetation types, slopes, and aspects within a hillslope at the East River  
 239 Watershed, which were used with obtained HPM estimates to explore how vegetation heterogeneity influences ET  
 240 and  $R_{ECO}$  dynamics. To perform this assessment, we computed the spatial distribution of vegetation types at watershed  
 241 scale based on Falco et al. (2019). We evaluated manually and selected 16 locations within the East River Watershed  
 242 having different vegetation types and slope aspects. These 16 locations were chosen to be at the center of vegetation  
 243 patched and covered by one vegetation type. A summary of the locations is presented in Table 2; the spatial distribution  
 244 of the locations is shown in Figure 2.

245 **Table 2: Location and vegetation types of East River Watershed sampling points (Figure 2)**

Easting (m)	Northing (m)	Vegetation Type	Aspect	Elevation (m)
327085	4309878	Deciduous Forest	South	2983
326288	4312504	Deciduous Forest	South	3177
330012	4313132	Deciduous Forest	North	3108
326854	4313192	Deciduous Forest	South	3098
328246	4312832	Meadow	South	3095
327010	4315059	Meadow	South	2790
328738	4306139	Meadow	North	2890
334270	4309465	Meadow	North	2929
333406.5	4308340	Riparian Shrubland	South	2760
327846	4312497	Riparian Shrubland	South	2723
334641	4305632	Riparian Shrubland	North	2740
330760	4310097	Riparian Shrubland	South	2855
329573	4314569	Evergreen Forest	South	3026
333106	4307313	Evergreen Forest	North	3102
325056	4310456	Evergreen Forest	South	2961
335141	4309614	Evergreen Forest	North	3131

246



247  
 248 **Figure 2: Vegetation classification of the East River, CO Watershed from Falco et al. (2019). East River sites selected in**  
 249 **this study are denoted by black circles.**

250 **2.4 Data Collection and Processing**

251 To enhance transferability of the developed HPM strategy to less intensively characterized watersheds, we  
252 selected only “easy to measure” or “widely available” attributes, such as precipitation, air temperature, radiation and  
253 NDVI, as inputs to the HTM model. Soil temperature was used when available. The data sources used for these inputs  
254 include FLUXNET data (<https://fluxnet.fluxdata.org/>), SNOTEL data (<https://www.wcc.nrcs.usda.gov/snow/>) and  
255 developed CLM model (Tran et al., 2019) at SNOTEL stations, DAYMET meteorological inputs (Thornton et al.,  
256 2017) and remote sensing data from Landsat imageries (Irons et al., 2012).

~~257 ——— A variety of measured data and model outputs were used to train and validate HPM. We obtained daily  
258 meteorological data, including air temperature, precipitation, radiation, ET, and  $R_{ECU}$  data, from the FLUXNET  
259 database at the selected FLUXNET sites. The pipeline of data processing for FLUXNET dataset is provided at  
260 <https://FLUXNET.fluxdata.org/>. We identified some data gaps and erroneous data (especially during winter seasons)  
261 for the ET estimates at US-NR1, which were cleaned following the procedures presented in Rungee et al. (2019). The  
262 meteorological data were used as inputs for HPM development, and ET and  $R_{ECU}$  data from these sites were used for  
263 HPM validation. At the three selected SNOTEL stations, we obtained air temperature, precipitation, and snow-water-  
264 equivalent data from the SNOTEL database. Air temperature data at these three SNOTEL stations were processed  
265 following Oyler et al. (2015), given potential systematic artifacts. Snow-water equivalent data are not easily acquired,  
266 and thus were not considered as inputs for HPM. However, a categorical variable was constructed to assimilate  
267 information regarding snow (Section 3.2.1). CLM models were generated following Tran et al. (2019) for the  
268 SNOTEL stations and US-NR1 to assess the spatiotemporal variability of ET at the East River Watershed and for  
269 training and validating HPM (Section 4.3). The DAYMET dataset (Thornton et al., 2017) provided gridded daily  
270 weather forcings attribute estimates at a 1 km spatial resolution. We obtained the incident radiation data from  
271 DAYMET at the SNOTEL stations as inputs for HPM. For the East River Watershed sites, meteorological forcings  
272 data, including air temperature, precipitation and radiation, were also obtained from DAYMET. The low spatial  
273 resolution of DAYMET data introduces uncertainty in HPM estimation of ET and  $R_{ECU}$ , which will be discussed in  
274 the following sections. We calculated the NDVI time series from the red band (RED) and near-infrared band (NIR)  
275 from Landsat 5, 7, and 8 images at all selected FLUXNET sites, SNOTEL stations, and East River Watershed sites at  
276 a spatial scale of 30 m.~~

277 Since cloud conditions can severely decrease data quality, we and radiation data was obtained from  
278 DAYMET. CLM models were generated following Tran et al. (2019) for the SNOTEL stations and US-NR1. At the  
279 East River Watershed sites, data were obtained from DAYMET. NDVI time series were calculated from the red band  
280 and near-infrared band from Landsat 5, 7 and 8 images at all sites. We used the cloud-scoring algorithm provided in  
281 the Google Earth Engine to mask clouds in all retrieved data, only selecting the ones that had a simple cloud score  
282 below 20 to ensure data quality. Given the different calibration sensors used in Landsat 5, 7, and 8, we also followed  
283 the processes described in Homer et al. (2015) and Vogelmann et al. (2001) to keep NDVI computations consistent  
284 over time. Landsat satellites have a return period of 16 days, and thus we performed a reconstruction of NDVI time  
285 series to obtain daily scale time data (Section 3.2.2).

Formatted: Indent: First line: 0.5"

286 **3. Hybrid Predictive Modeling Framework**

287 In this section, we illustrate the steps for building an HPM model for ET and  $R_{ETC}R_{eco}$  estimation over time  
288 and space. Figure 3 presents the general framework of HPM, which includes modules for data preprocessing, model  
289 development, model validation, and predictive modeling.

290 **3.1 Model Framework**

291 \_\_\_\_\_ HPM establishes relationships among meteorological forcings attributes, NDVI, ET, and  
292  $R_{ETC}R_{eco}$  (Figure 3). Both input data (e.g., meteorological forcings) and output data (ET and  $R_{ETC}$ ) used for training  
293 and validation are preprocessed for gap filling, smoothing, and data updating. HPM “learns” the complex space-time  
294 relationship among meteorological forcings, NDVI, ET, and  $R_{ETC}$  using a deep-learning-based module (deeply fully  
295 connected deep neural networks and a long short-term memory recurrent neural network). HPM then can be used for  
296 ET and  $R_{ETC}$  estimation at sparsely monitored watersheds. Individual HPM models can be trained in two different  
297 ways using ET and  $R_{ETC}$  information: with data obtained from flux towers (“data-driven HPM”) or with outputs from  
298 1-D physically-based models (“mechanistic HPM”). In both cases, the models obtained with local data are then used  
299 to estimate ET and  $R_{ETC}$  at other sites in the same ecoregion (see Section 2.1). For ecoregions not represented by  
300 FLUXNET sites, it is necessary to develop mechanistic HPM that enables ET and  $R_{ETC}$  estimation over space and  
301 time.

302 \_\_\_\_\_ HPM has several additional modules, including model development, model validation, and model  
303 prediction modules. In the HPM model development module, deep learning algorithms are trained with input features  
304 and response data until a pre-defined “stopping criteria” (e.g., root mean squared error, RMSE) is met, indicating  
305 subsequent training would lead to minimal improvement. In the validation module, estimation outputs from the  
306 “trained HPM models” are compared with other ET and  $R_{ETC}$  data obtained from other independent sites or  
307 mechanistic models within the same ecoregion. Statistical measures, including adjusted  $R^2$  and mean absolute error  
308 (MAE), are computed to evaluate the performance of HPM models. In the predictive model module, meteorological  
309 forcings data and remote sensing data are processed at target sites of interest, and the validated HPM model is used to  
310 estimate ET and  $R_{ETC}$  at these sites. ET and  $R_{ETC}$  outputs estimated from HPM at sparsely monitored watersheds then  
311 provide alternative datasets for process understanding within the target watersheds.

Formatted: Indent: First line: 0.5"

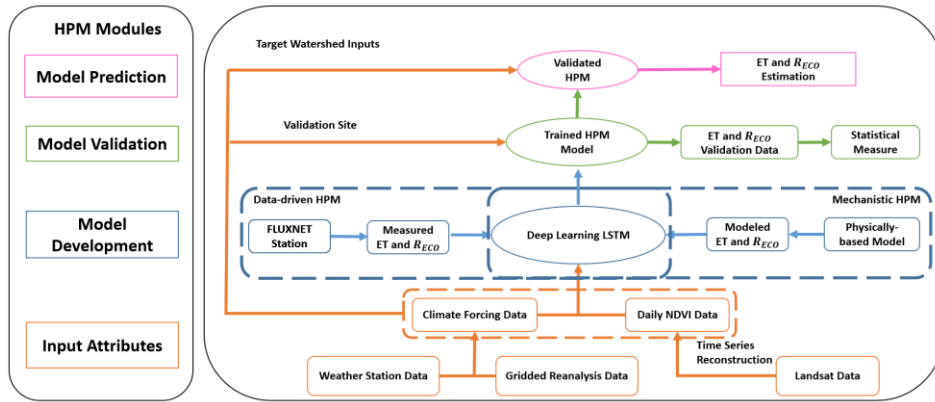


Figure 3: Hybrid Predictive Model (HPM) Framework. The HPM model mainly consists of four modules: Input Attributes, Model Development, Model Validation and Model Prediction, represented by rectangles with colors. Arrows represent the linkages among different modules. Choices of data-driven HPM or mechanistic HPM depend on the ecoregion of target watershed and data availability.

Long short-term memory (LSTM, Hochreiter & Schmidhuber, 1997) is capable of identifying long-term dependencies between climate and environmental data; a type of recurrent neural network (RNN) capable of learning temporal dependence without suffering from optimization difficulties (e.g., vanishing errors). An LSTM layer consists of memory blocks and unique cell states that are controlled by three multiplicative units, including the input, output and forget gates. These gates regulate the flow of information and decide which data in a sequence is important to keep or throw away. Through the LSTM structure, even information from the earlier time steps can make its way to later time steps, reducing the effects of short-term memory and thus capturing long-term dependence. LSTM has been previously used to capture such dependencies between climate and environmental data. For example, Kratzert et al. (2018) successfully used LSTM to learn the long-term dependencies in hydrological data (e.g., storage effects within catchments, time lags between precipitation inputs and runoff generation) for rainfall-runoff modeling. LSTM has also been used for gap filling in hydrological monitoring networks in the spatiotemporal domain (Ren et al., 2019). In this study, the outputs (ET or  $R_{ECO}$ ) denoted as  $y$  are predicted from the input  $x = [x_1, x_2, \dots, x_T]$ , consisting of the last  $T$  consecutive time steps of attributes, such as meteorological forcings attributes (e.g., air temperature and precipitation) and remote sensing attributes (i.e., NDVI). In a recurrent neural network (RNN),  $h_t$  represents the internal state at every time step  $t$  that takes in current input value  $x_t$  and previous internal state  $h_{t-1}$ , and is recomputed along the time axis using the following equation. More information about the LSTM-RNN method is provided by Olah (2015).

$$h_t = g(Wx_t + Uh_{t-1} + b), \quad (1)$$

where  $g$  represents the hyperbolic tangent activation function,  $W$  and  $U$  are trainable weight matrices of the hidden state  $h$ , and  $b$  is a bias vector.  $W$ ,  $U$  and  $b$  are all trainable through optimization. LSTM introduces the cell state  $c_t$ ,

Formatted: Indent: First line: 0"

337 which makes LSTM powerful in identifying long-term dependencies in a statistical manner. The cell state  $c_t$  has three  
 338 gates—structures, including “forget gates” (which determine what information from previous cell states will be  
 339 forgotten), “HPM modules include input gates” (which determine what information will be conveyed from the forget  
 340 gate) and “output gates” (which return information from cell state  $c_t$  to a new state  $h_t$ ). With these gate structures, the  
 341 cell state  $c_t$  controls what information will be forgotten, conveyed, and updated over time. The forget gate is  
 342 formulated as follows:

$$343 \quad f_t = \sigma(W_f x_t + U_f h_{t-1} + b_f), \quad (2)$$

344 where  $f_t$  results in a value between 0 and 1 indicating the degree of information to be forgotten;  $\sigma$  is the logistic  
 345 sigmoid function, and  $W_f, U_f$  and  $b_f$  are trainable parameters. Next, the input gate decides which values will be  
 346 updated in the current cell state, and creates a vector of candidate values  $\tilde{c}_t$  in the range of  $(-1, 1)$  through a  $\tanh$  layer,  
 347 which will be used to update the current state. With the candidate values calculated from the current state, and the  
 348 information conveyed from the forget gate, we can calculate the current cell state as follows:

$$349 \quad i_t = \sigma(W_i x_t + U_i h_{t-1} + b_i), \quad (3)$$

$$350 \quad \tilde{c}_t = \tanh(W_c x_t + U_c h_{t-1} + b_c), \quad (4)$$

$$351 \quad c_t = f_t * c_{t-1} + i_t * \tilde{c}_t, \quad (5)$$

352 where  $i_t$  is the input gate that defines which information of  $\tilde{c}_t$  will be used to update the current cell state and is in the  
 353 range of  $(0, 1)$ ;  $c_t$  represents the current cell state; and  $W_c, U_c, b_c, W_i, U_i$ , and  $b_i$  are trainable parameters. Finally, the  
 354 output gate  $o_t$  controls the information of cell state  $c_t$  to a new hidden state  $h_t$ , which is computed using the following  
 355 equation:

$$356 \quad o_t = \sigma(W_o x_t + U_o h_{t-1} + b_o), \quad (6)$$

$$357 \quad h_t = \tanh(c_t) * o_t, \quad (7)$$

358 With the new hidden state calculated, ET and  $R_{ETOT}$  can be calculated using a one-unit dense layer:

$$359 \quad y_t = W_d h_t + b_d, \quad (8)$$

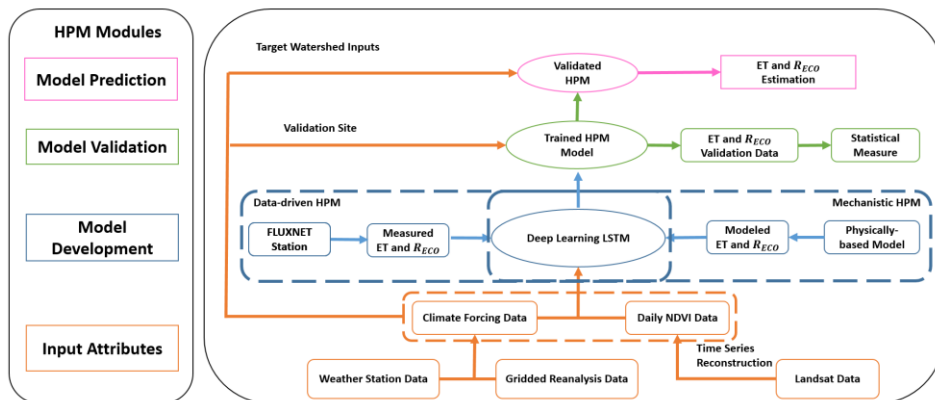
360 where  $W_d$  and  $b_d$  are additional trainable parameters. In summary, the LSTM unit calculates the internal state using  
 361 current meteorological forcings and remote sensing data at every time step. The forget gate, input gate, and output  
 362 gate decide what information from previous time steps will be kept, updated, and conveyed to the new hidden state.  
 363 Finally, with a single dense layer, the algorithm will output ET and  $R_{ETOT}$  estimation from the trained `attributes` model:

364 A 70%–30% split between training and development, validation time-series, and prediction. Based on data  
 365 availability, input features are obtained from flux towers, gridded meteorological data was applied here, where the  
 366 first 70% of the data were used, and remote sensing data; all data are preprocessed for gap filling, smoothing, and  
 367 updating. In the HPM model development as a learning process, and 30% of the data were used as validation sets

Formatted: Indent: First line: 0.5"

368 at module, individual sites. At the East River Watershed, HPM results were also validated. HPM models can be trained  
 369 in two different ways based on data availability: with data obtained from flux towers (“data-driven HPM”) or with  
 370 benchmark CLM outputs from physically-based models (“mechanistic HPM”). Seventy percent of these data are used  
 371 for training LSTM to learn the interactions among input features, ET, and  $R_{eco}$ , until a pre-defined “stopping criteria”  
 372 (e.g., root mean squared error, RMSE) is met, indicating subsequent training would lead to minimal improvement.  
 373 Tran et al. (2019) and FLUXNET measurements. We used the mean absolute error (MAE), and adjusted  $R^2$  as the  
 374 statistical measure to determine model performance. In most models, the configuration of the neural networks includes  
 375 a first LSTM layer with 50 units, a second LSTM layer with 25 units, and a dense layer with 8 units having L2  
 376 regularizers, and a final output dense layer. Dropout layers are also embedded in the model to prevent overfitting.  
 377 There are 11600 and 7600 parameters for the first and second LSTM layers; 208 and 9 for the first and second dense  
 378 layers and no parameters for the dropout layers. Other configurations of networks may provide better estimation results;  
 379 however, they are not assessed in this study as the proposed configuration already provide reasonable results. More  
 380 information about the LSTM-RNN method is provided by Olah. (2015).

381 In the validation module, we implemented a validation procedure that uses the remaining 30 % of the data to  
 382 assess model performance. Estimation outputs from the trained HPM models are also compared with other ET and  
 383  $R_{eco}$  data obtained from other independent sites or mechanistic models within the same ecoregion. Statistical measures  
 384 such as adjusted  $R^2$  and mean absolute error (MAE) are computed to evaluate the performance of HPM models. In  
 385 the predictive model module, meteorological forcings data and remote sensing data are processed at target sites of  
 386 interest, and the validated HPM model is used to estimate ET and  $R_{eco}$  at these sites. ET and  $R_{eco}$  outputs estimated  
 387 from HPM at sparsely monitored watersheds then provide alternative datasets for process understanding within the  
 388 target watersheds.



389  
 390 **Figure 3: Hybrid Predictive Model (HPM) Framework.** The HPM model mainly consists of four modules: **Input Attributes,**  
 391 **Model Development, Model Validation and Model Prediction,** represented by rectangles with colors. Arrows represent the

392 linkages among different modules. Choices of data-driven HPM or mechanistic HPM depend on the ecoregion of target  
393 watershed and data availability.

### 394 3.2 Feature Selection

395 ~~Key properties influencing ET and  $R_{veg}$  dynamics are linked to snow processes, plant dynamics, moisture~~  
396 ~~stresses, radiation inputs and other relevant processes. However, at At sparsely monitored watersheds, only~~  
397 ~~weather reanalysis data and remote sensing data are commonly available. Thus, we mainly considered air temperature,~~  
398 ~~radiation, precipitation, vegetation indices (e.g., NDVI) and variables inferred from these data as inputs for HPM. Soil~~  
399 ~~temperature when available is used at FLUXNET sites.~~ Other key attributes that depend on depth and site-specific  
400 characteristics such as soil moisture and snow depth are not used in current HPM models due to data availability.

#### 401 3.2.1 Snow information

402 In ~~snow-influenced~~ mountainous watersheds, ~~snow dynamics significantly influence water and carbon fluxes.~~  
403 ~~Because of the difficulties in measuring snow time series over space, we did not directly use attributes such as snow~~  
404 ~~water equivalent as input to HPM. Instead,~~ we separated precipitation data into snow precipitation (when air  
405 temperature < 0) and rainfall precipitation (when air temperature > 0). ~~This, which~~ is in line with what has been used  
406 in hydrological models such as CLM (Oleson et al., 2013). ~~Note that for certain sites in this study, snow is not present~~  
407 ~~(e.g., US Ton). In order to capture the dynamics of snow processes, such as accumulation and melting, we constructed~~  
408 ~~a categorical variable ( $sn$ ), as follows: Knowles et al. (2016) discovered a significant correlation between day of peak~~  
409 ~~snow accumulation, snowmelt and air temperature. To capture snow related dynamics (e.g., snowmelt), we constructed~~  
410 ~~a categorical variable ( $sn$ ) based on air and soil temperature thresholds. Note: this may not be needed if snow data~~  
411 ~~becomes available and at sites where snow is rarely present.~~

$$412 \quad sn = \begin{cases} 0, \text{ during snow accumulation; } SWE > 0 \text{ and } SWE < \text{peak } SWE \\ 1, \text{ during snow melting; } SWE > 0 \text{ and } SWE \leq \text{peak } SWE \\ 2, \text{ no snow; } SWE = 0 \end{cases}, \quad (9)$$

413 Since data on peak SWE are rarely available because of the difficulties in measuring snow, we also define a  
414 proxy categorical variable,  $sn$ . When no SWE measurements were available, we estimated  $sn$  using air and soil  
415 temperature data following Knowles et al. (2016), who found significant correlations between the day of peak snow  
416 accumulation and first day of air temperature above 0 degrees Celsius, as follows:

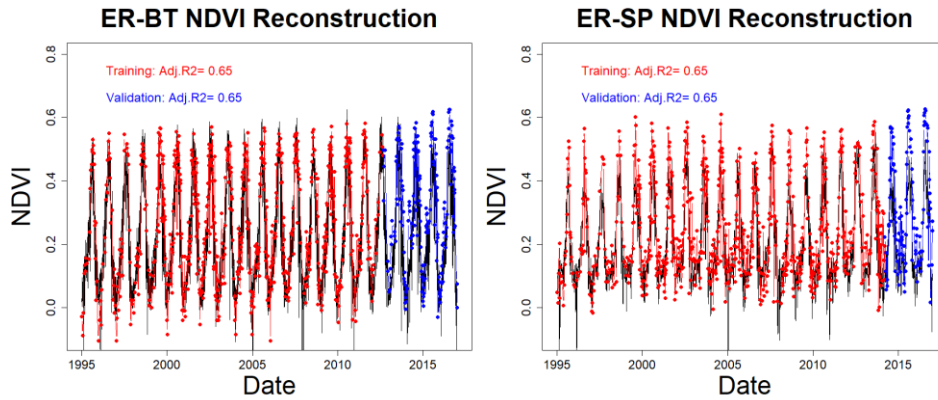
$$417 \quad sn = \begin{cases} 0, \text{ during snow accumulation; Air Temperature } < 0 \\ 1, \text{ during snow melting; Air Temperature } > 0 \text{ while Soil Temperature } \leq 0, \\ 2, \text{ no snow; Air Temperature and Soil Temperature } > 0 \end{cases}, \quad (10)$$

#### 418 3.2.2 Vegetation information

419 ~~To mitigate the long return periods of satellites and the presence of clouds, we We reconstructed daily~~  
420 ~~NDVI values based on meteorological foreingsforcing data (e.g., air temperature, precipitation, radiation) using deep-~~  
421 ~~learning recurrent neural networks, leading LSTM to estimates of NDVI at daily increase the temporal resolution. For~~  
422 ~~example, coverage of NDVI.~~ Figure 4 represents Landsat-derived NDVI and reconstructed NDVI values for two sites



423 at the East River, CO watershed: Butte (ER-BT), and Schofield Pass (ER-SP). Figure 4 reveals that based on  
424 meteorological forcings data only, the reconstructions achieved an adjusted  $R^2$  of 0.65. Though not ideal, as satellites  
425 continue to advance and more training data becomes available, the accuracy of NDVI temporal reconstruction is  
426 expected to increase.



427  
428 **Figure 4: Temporal reconstruction of NDVI at ER-BT (left) and ER-SP (right). Black lines represent reconstructed daily**  
429 **NDVI. Red points are used for training and blue points are used for validation**

### 430 3.3 Use Cases

431 We developed four different use cases to demonstrate the applicability of HPMs based on site-specific data  
432 and model availability. Use case 1 focuses on ET and  $R_{eco}$  in the time domain, where a HPM is trained on direct  
433 measurements from flux tower. A 70%-20%-10% training-validation-prediction split of the data was used. These  
434 HPMs are useful for time series gap filling and future prediction. Use case 2 and use case 3 have emphasis on providing  
435 ET and  $R_{eco}$  over space, where use case 2 uses data-driven HPM and use case 3 utilizes mechanistic HPM. Data-driven  
436 HPM is trained with data from flux tower and mechanistic HPM is trained upon outputs from a mechanistic model  
437 (e.g., CLM). These HPMs are usually trained at well monitored watersheds where either flux data is available or data  
438 support the development of a mechanistic model. After training, these HPMs integrate meteorological and remote  
439 sensing inputs to provide ET and  $R_{eco}$  at target sparsely monitored watersheds within the same ecoregion. For both  
440 use case 2 and 3, we validated the HPM estimations against data from other sites within the same ecoregion. Use case  
441 4 focuses on the East River Watershed, where we demonstrate how HPM can increase our understanding of ecosystem  
442 fluxes and explore the limitations of HPM in mountainous watersheds. Use case 4 estimations were validated against  
443 data extracted from other studies.

## 444 4. Results

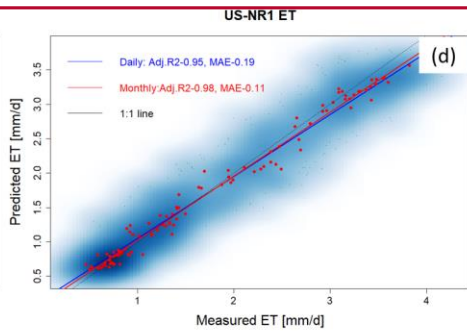
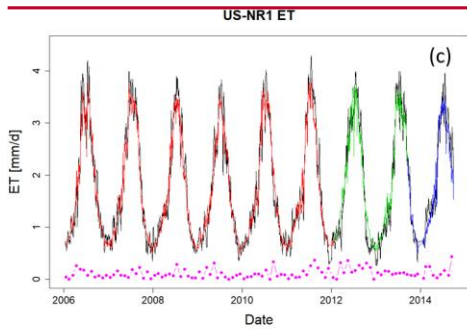
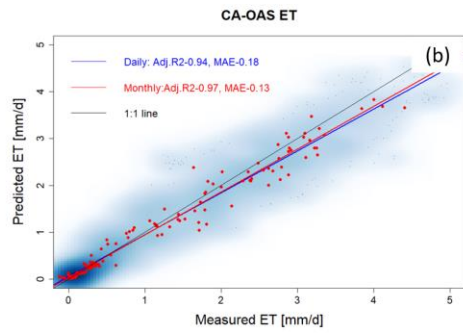
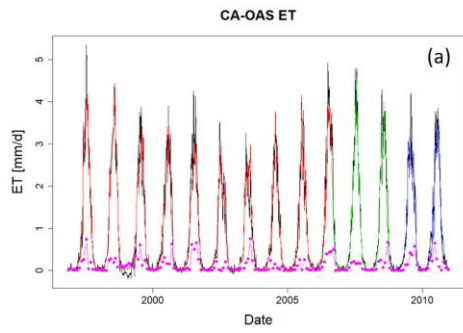
445 We tested HPM's capabilities using four different use cases to explore different conditions. First, we tested  
446 the capability of HPM to estimate long term temporal dependency among meteorological forcings, ET, and  $R_{eco}$  (Use  
447 Case 1; presented in Section 4.1). Second, we validated HPM's capability to estimate the spatial distribution of ET

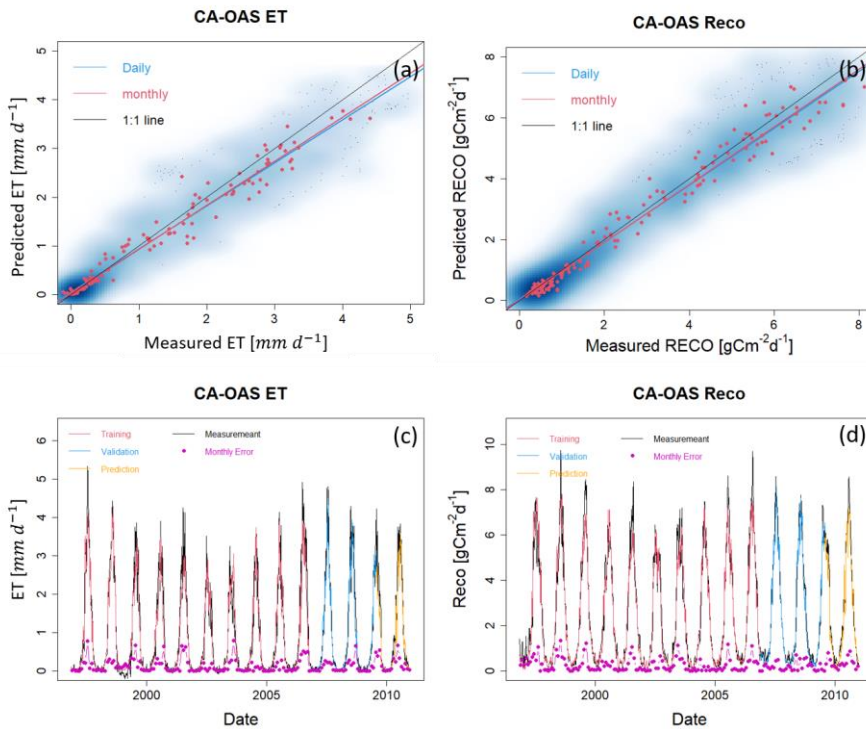
448 and  $R_{eco}$  over space in selected watersheds, where we developed HPM using existing FLUXNET data (Use Case 2;  
449 data-driven HPM, Section 4.2) or outputs from a mechanistic model (Use Case 3; physical model-based HPM, Section  
450 4.3). In Use Case 4, HPM was used to estimate ET and  $R_{eco}$  at selected sites within the East River Watershed and to  
451 distinguish how ET and  $R_{eco}$  dynamics varies in the East River Watershed (Section 4.4). Temporal resolution of HPM  
452 models for all Use Cases are at daily scale and the spatial resolution depends on the use of meteorological forcing data.  
453 These four use cases illustrate and demonstrate how HPM can be developed and applied at target watersheds where  
454 data are sparse.

#### 455 4.1 Use Case 1: ET and $R_{eco}$ Time Series Estimation with HPM Developed at FLUXNET Sites

456 Local HPMs were developed to estimate ET and  $R_{eco}$  using flux tower data obtained from FLUXNET  
457 sites listed in Table 1. At all FLUXNET sites, air temperature, precipitation, net radiation, NDVI and soil temperature  
458 were used. For US-NR1, CA-Oas and CA-Obs,  $\gamma$  is also included. The results, which are shown in Figure Fig. 5, A1-  
459 A4 and Table 3, reveal that the HPM approach was effective for estimating ET. Adjusted  $R^2$  between the HPM  
460 estimates and flux tower measurements are above 0.85 for all sites, and mean absolute errors are small at a level of  
461  $\sim 0.2$  mm/d. Figure 5 displays the daily scale estimation of ET from HPM US-NR1 and CA-OAS (other sites provided  
462 in supplementary material), and presents monthly mean ET values of measurements, HPM estimations, and  
463 differences  $R_{eco}$ . The long-term trends in ET and  $R_{eco}$  are well captured by HPM. At larger temporal scales (monthly  
464 or yearly), HPM provides reasonable estimation of ET at these sites. However, short-term fluctuations in ET and  $R_{eco}$   
465 during the summer periods are also not well captured by ET, specifically at California sites during the periods when  
466 plant transpiration HPM. For example, at US-Ton and US-Var, we observed an increasing discrepancy in summer  
467 month ET and  $R_{eco}$ . This is mainly caused by insufficient training for summer extremes. At US-Me2, we observed  
468 significant increasing errors in the validation set, especially for  $R_{eco}$  that are caused by significant differences in raw  
469 data between 2002-2010 (data used for training) and soil evaporation are constrained by soil moisture (Figure A2  
470 panel a post-2011 (data used for validation)).

Formatted: Font: Italic



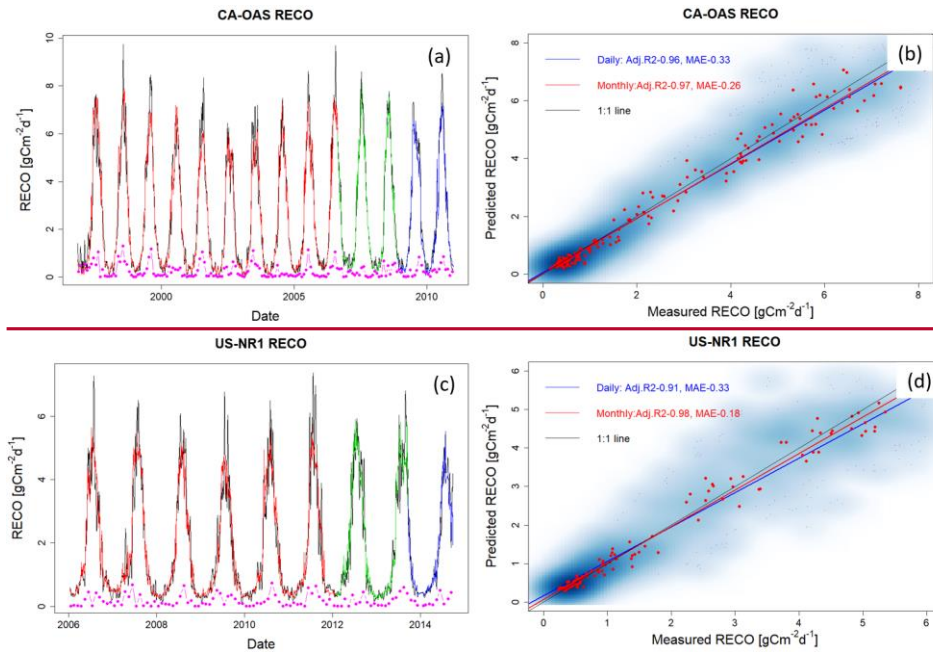


472  
 473 **Figure 5: ET and  $R_{eco}$  estimation with data from FLUXNET sites at CA-OAS and US-NRI. Panels (a) and (c) illustrate the**  
 474 **daily estimation of ET with red, green, and blue lines representing data used for training, validation, and prediction,**  
 475 **respectively, and the black line showing the eddy covariance measurements. Pink points describe monthly mean difference**  
 476 **between HPM estimation and measured data. Panels (b) and (d) show the scatter plots of daily (blue) and monthly (red)**  
 477 **ET, and  $R_{eco}$  between HPM estimation and FLUXNET data. Darker blue clouds represent greater density of data points.**  
 478 **Panels (c) and (d) present the daily HPM estimation of ET and  $R_{eco}$  separated by training, validation and prediction sets.**  
 479 **Pink points depict monthly error between HPM estimation and FLUXNET data. Results for other sites are included in**  
 480 **supplementary materials below (Figures Fig. A1 and A2).**

481 — Similarly, Table 3 and Figure 6 reveal that HPM was also effective in estimating  $R_{eco}$ , leading to small MAE  
 482 and adjusted  $R^2$  of 0.8 between estimated and measured  $R_{eco}$  except for US-Ton and US-Var. Figure 6 presents HPM-  
 483 estimated  $R_{eco}$  at US-NRI and CA-OAS, with other sites presented in Figures A3 and A4. Long-term dynamics of  
 484  $R_{eco}$  are also successfully captured by HPM; however, HPM does not accurately capture  $R_{eco}$  during peak growing  
 485 seasons. For example, we observed an over-estimation of  $R_{eco}$  during 2012 summer at US-Whs, whereas at US-NRI  
 486 HPM estimation during peak growing season are smaller than measured values. While soil moisture is important for  
 487  $R_{eco}$  during peak growing season (Ng et al., 2014; Wang et al., 2014), the developed HPM currently does not include  
 488 soil moisture as a key attribute. HPM  $R_{eco}$  estimation at US-Ton and US-Var show higher uncertainties (i.e., MAE  $\rightarrow$

Formatted: Font: 9 pt, Bold

489 0.4 and Adj.  $R^2 < 0.9$ ). At these sites limited by water conditions (e.g., US Ton) and sites with seasonally dry periods  
 490 (e.g., US Whs), it is necessary to include variables that could provide information regarding moisture stresses in the  
 491 subsurface. Soil moisture that directly quantify water stress can be helpful to increase  $R_{ECO}$  prediction accuracy  
 492 (Noormets et al., 2008). Underestimation of peak growing season  $R_{ECO}$  can also come from biases within LSTM  
 493 training, which is strong in capturing long term temporal trends but less effective in obtaining peak values, and thus  
 494 lead to increasing prediction errors during growing season compared to other periods of time.



495  
 496 **Figure 6:**  $R_{ECO}$  estimation with data from FLUXNET sites at CA-OAS and US-NR1. Panels (a) and (c) present daily  
 497 estimation of  $R_{ECO}$  with red, green, and blue lines representing data used for training, validation, and prediction, and the  
 498 black line shows the eddy covariance measurements. Pink points describe monthly mean difference between HPM  
 499 estimation and measured data. Panels (b) and (d) show the scatter plots of daily (blue) and monthly (red)  $R_{ECO}$ . Darker  
 500 blue clouds represent greater density of data points. Results for other sites are included in supplementary materials below  
 501 (Figures A3 and A4).

502 **Table 3:** Statistical measures of HPM estimation of ET and  $R_{ECO}R_{eco}$

Site ID	Train MAE -ET [mm /dt d <sup>-1</sup> ]	Test MAE -ET [mm /dt d <sup>-1</sup> ]	Train Adj. R <sup>2</sup> - ET	Test Adj. R <sup>2</sup> - ET	Train MAE $-R_{ECO}R_{eco}$ [gCm <sup>-2</sup> d <sup>-1</sup> ]	Test MAE $-R_{ECO}R_{eco}$ [gCm <sup>-2</sup> d <sup>-1</sup> ]	Train Adj. R <sup>2</sup> $-R_{ECO}R_{eco}$	Test Adj. R <sup>2</sup> $-R_{ECO}R_{eco}$
US-NR1	0.19	0.11	0.95	0.98	0.33	0.18	0.91	0.98
CA-Oas	0.18	0.13	0.94	0.97	0.33	0.26	0.96	0.97
CA-Obs	0.12	0.09	0.95	0.96	0.29	0.25	0.96	0.97

Formatted: Subscript

Formatted Table

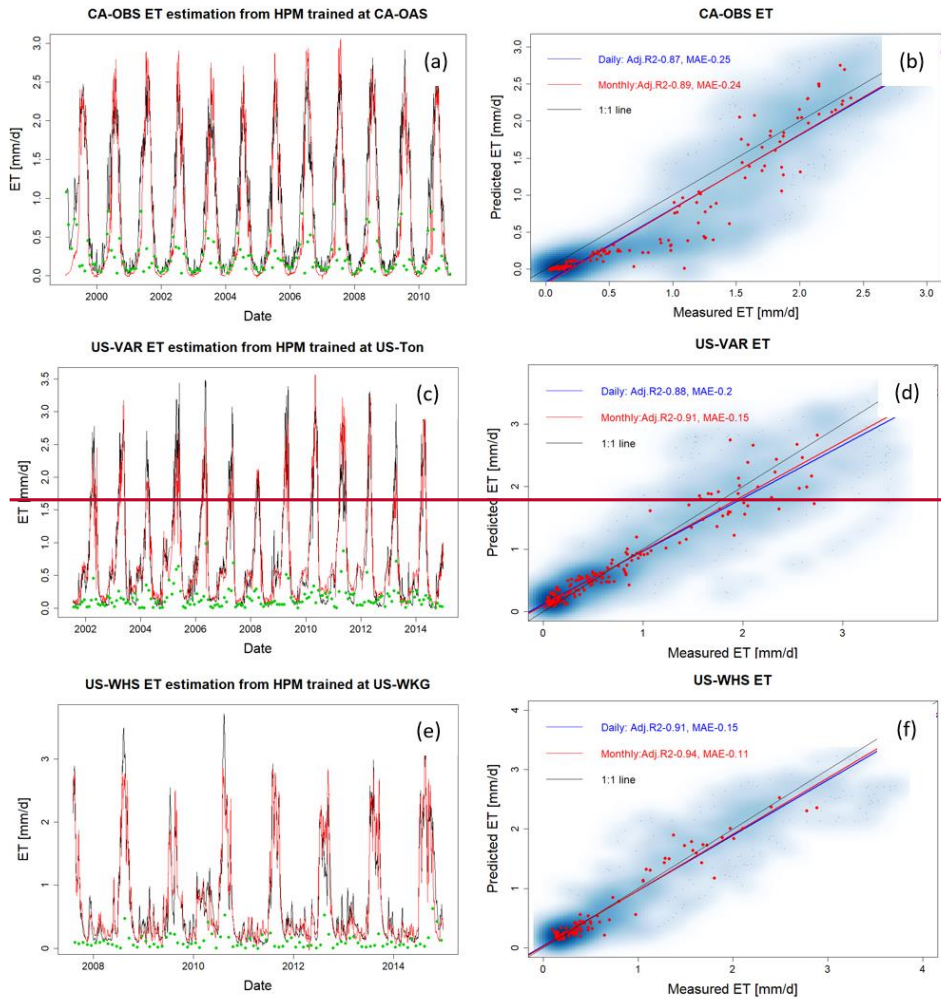
US-SRM	0.22	0.17	0.92	0.94	0.24	0.19	0.80	0.87
US-Ton	0.22	0.17	0.92	0.94	0.43	0.36	0.76	0.82
US-Var	0.15	0.12	0.92	0.95	0.49	0.38	0.81	0.88
US-Whs	0.13	0.09	0.93	0.96	0.12	0.09	0.84	0.89
US-Wkg	0.19	0.15	0.87	0.91	0.18	0.15	0.85	0.91
US-Me2	0.36	0.43	0.81	0.75	0.75	0.83	0.88	0.85

503

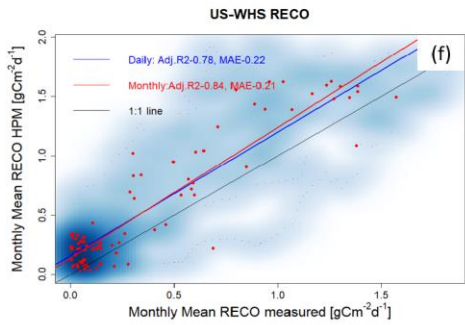
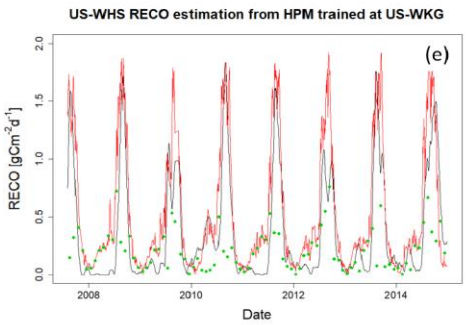
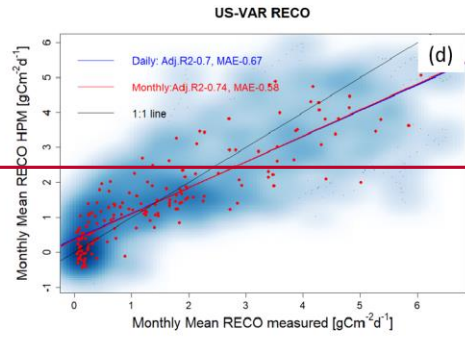
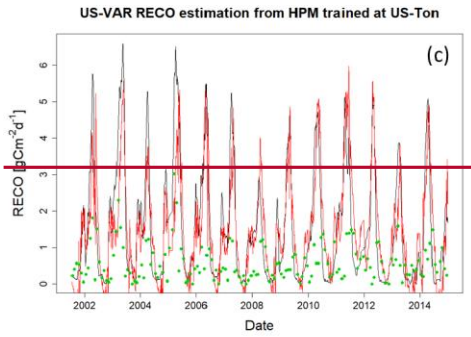
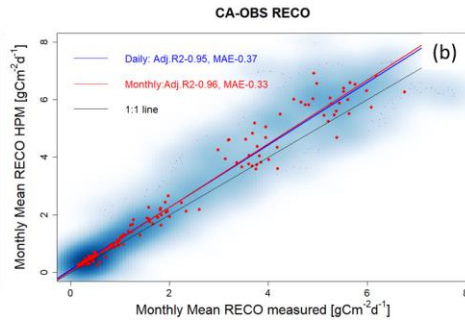
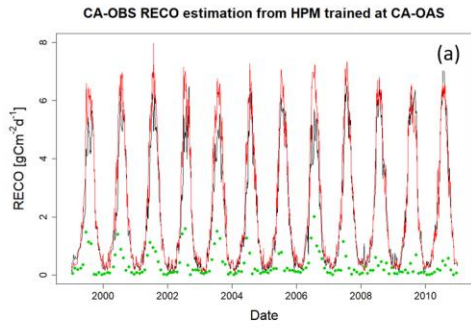
#### 504 4.2 Use Case 2: Ecoregion-Based, Data-Driven HPM Model for ET and $R_{ECO}$ Estimation

505 ~~While the effort and cost involved in establishing flux towers naturally limit the spatial coverage of obtained~~  
506 ~~measurements, point scale measurements from one FLUXNET station provides representative information about~~  
507 ~~ecosystem dynamics at other locations within the same ecoregion.~~ In this section, we explored the use of a data-driven  
508 HPM trained with one FLUXNET station to estimate ET and  $R_{ECO}$  at other locations within the same ecoregion.  
509 ~~To test this approach, we first trained HPM at a selected FLUXNET stations and validated these HPM models at other~~  
510 ~~FLUXNET stations (ET and  $R_{ECO}$  data at testing sites were only used for comparison with HPM prediction) within~~  
511 ~~the same ecoregion.~~ Specifically, we developed HPM models at US-Ton, CA-Oas and US-Wkg, and provided ET and  
512  $R_{ECO}$  estimations at US-Var, CA-Obs and US-Whs at three ecoregions, respectively.

513 Table 4 summarizes how we developed the data-driven HPM models for spatially distributed estimation of  
514 ET and  $R_{ECO}$  as well as the corresponding statistical summaries. Figures 76 and 8A5 present the time series of  
515 HPM-estimated ET and  $R_{ECO}$  compared to measurements from flux towers. HPM estimation at US-Obs, US-Whs and  
516 US-Var achieved an adjusted  $R^2$  of 0.87, 0.88 and 0.91 for ET and 0.95, 0.70 and 0.78 for  $R_{ECO}$ , respectively. These  
517 results show that HPM captures the seasonal and long-term dynamics of ET and  $R_{ECO}$ . However, at sites that  
518 experience seasonally dry periods (e.g., US-Whs), prediction accuracy decreases during the peak growing season. ~~For~~  
519 ~~example, we observed large errors in HPM based estimations compared to measurements during peak growing~~  
520 ~~seasons (e.g., a 0.5 mm discrepancy in June mean ET). We interpret this discrepancy as the result that current HPM~~  
521 ~~models did not capture water stress conditions, and it is necessary to include other key attributes (e.g., soil moisture)~~  
522 ~~to improve prediction accuracy, especially at these sites with seasonally dry periods.~~ Although the prediction accuracy  
523 is not as high as Use Case 1 (Section 4.1), this use case demonstrates that HPM can learn the complicated relationships  
524 between responses and features successfully, and that a local data-driven HPM can be used to fuse with data from  
525 other subsites for long-term estimation of ET and  $R_{ECO}$  within the same ecoregions.

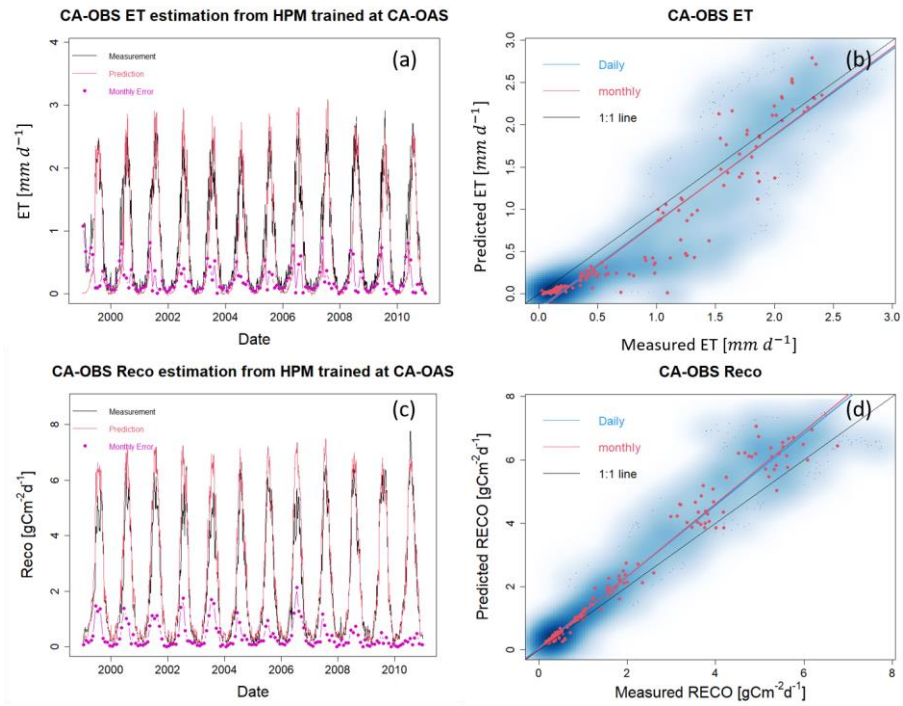


526  
 527 **Figure 7. ET estimation at CA-Oas (a), US-Var (c), and US-Whs (e) with HPM trained at US-Ton, US-Wkg, and CA-Oas,**  
 528 **respectively. Red and black lines represent HPM estimation and real measurements, with green points denoting the monthly**  
 529 **mean difference between HPM estimations and measurements. Panels (b), (d), and (f) show the scatter plots of daily (blue)**  
 530 **and monthly (red) ET at these three sites. Darker blue clouds represent greater density of data points.**





532 **Figure 8.  $R_{ETCO}$  estimation at CA-Oas (a), US-Var (c), and US-Whs (e) with HPM trained at US-Ton, US-Wkg, and CA-**  
 533 **Oas,**



534  
 535 **Figure 6. ET and  $R_{ECO}$  estimation at CA-Obs using HPM trained at CA-Oas. Other sites are presented in Fig. A5,**

536 **respectively. Red and black lines represent HPM estimations and real measurements; green points denote the monthly**  
 537 **mean difference between HPM estimation and measurements. Panels (b), (d), and (f) show the scatter plots of daily (blue)**  
 538 **and monthly (red)  $R_{ECO}$  at these three sites. Darker blue clouds represent greater density of data points.**

539 **4.3 Use Case 3: Ecoregion-Based, Mechanistic HPM Estimation of ET**

540 Mechanistic HPM, which is trained with ET estimates from 1-D physically-based model simulations,  
 541 provides an avenue for estimating ET in ecoregions where direct measurements from eddy covariance tower are not  
 542 available. In order to test the effectiveness of the mechanistic HPM, we focused on the three SNOTEL stations and  
 543 US-NR1, which locates in the “Western Cordillera” ecoregion. Mechanistic HPM is coupled with CLM simulations  
 544 at these sites (Tran et al., 2019). To ensure the CLM physically-based model simulations can provide alternative  
 545 datasets to develop mechanistic HPMs, we compared CLM estimation and direct measurements of ET at US-NR1  
 546 (Figure S2). The consistent results between measured ET and CLM-estimated ET (adjusted  $R^2 = 0.88$ ;  $k = 0.95$ )  
 547 indicate independent CLM simulations can be effectively used to develop the mechanistic HPM.

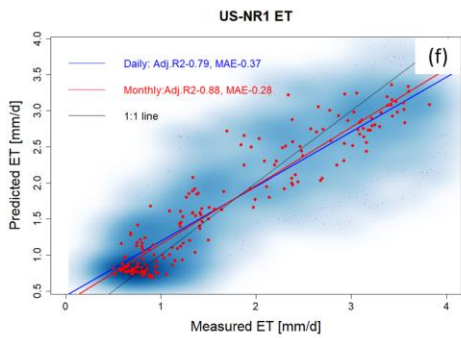
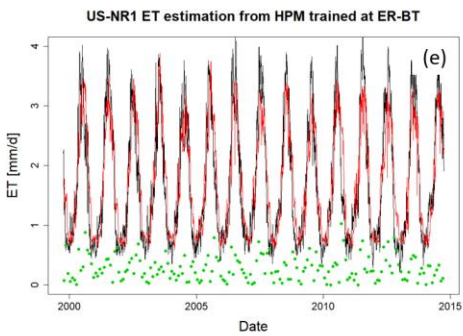
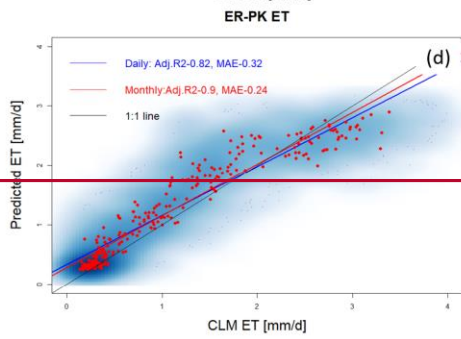
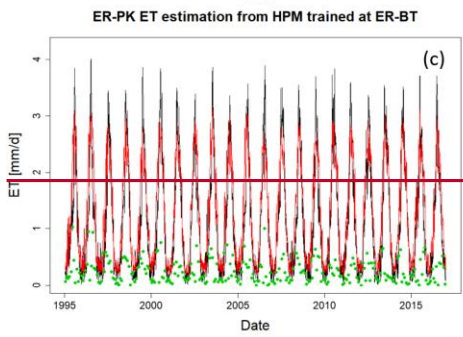
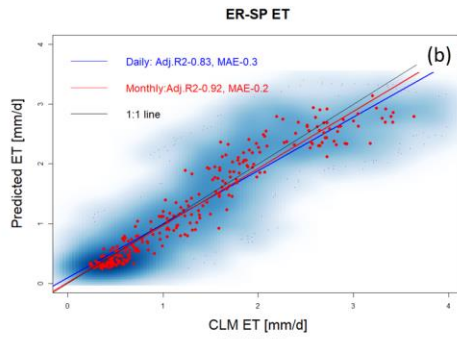
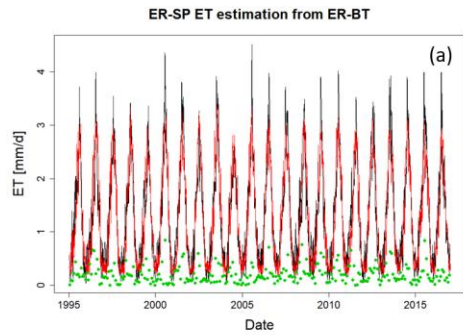
Formatted: Font: 10 pt, Not Bold

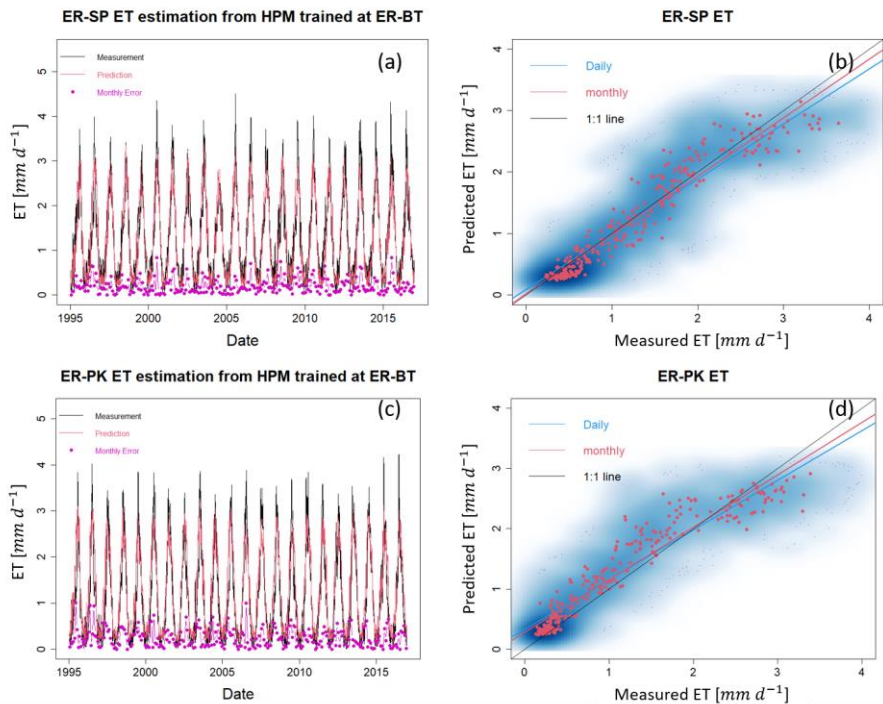
548 ~~We applied mechanistic HPM trained with 1-Dupon physically-based model simulations, provides an avenue~~  
 549 ~~for estimating fluxes in ecoregions where flux towers are not available. Consistent results between measured ET and~~  
 550 ~~CLM-estimated ET at US-NR1 (adjusted  $R^2 = 0.88$ ;  $k = 0.95$ , Fig. S1) indicate independent CLM simulations can~~  
 551 ~~be effectively used to develop the mechanistic HPM. We applied mechanistic HPM trained with 1-Dimensional~~  
 552 ~~(vertical) CLM developed at ER-BT (Tran et al., 2019) to estimate ET at sites classified as part of the ~~samewestern~~~~  
 553 ~~Cordillera ecoregion (i.e., ER-SP, ER-PK and US-NR1). We then compared ET estimation from HPM to independent~~  
 554 ~~CLM-based ET estimations at ER-SP and ER-PK ~~and to direct measurements at US-NR1.~~ Figure 97 shows a high~~  
 555 ~~consistency between HPM estimation and the validation data. For all scenarios, an adjusted  $R^2$  of 0.8 or greater is~~  
 556 ~~observed (Table 4), which strongly indicates that mechanistic HPM can provide accurate ET estimation at sites of~~  
 557 ~~similar ecoregions. These results suggest the broad applicability of mechanistic HPM to estimate ET based on~~  
 558 ~~ecoregion characteristics. This approach is expected to be particularly useful for regions where flux towers are difficult~~  
 559 ~~to install or where measured fluxes are not representative of the landscape, such as in mountainous watersheds.~~

560 **Table 4. Statistical summary of HPM estimation over space with FLUXNET sites and SNOTEL stations with CLM**

Target Site	Training Site	Level II Ecoregion	ET MSE (monthly)[ $mm/d$ ]	ET Adj. $R^2$	<del><math>R_{eco}R_{eco}</math></del> MSE(monthly)[ $gCm^{-2}d^{-1}$ ]	<del><math>R_{eco}R_{eco}</math></del> Adj. $R^2$
CA-Obs	CA-Oas	Boreal Plain	0.39	0.88	0.36	0.97
US-Var	US-Ton	Mediterranean California	0.34	0.70	0.67	0.70
US-Whs	US-Wkg	Western Serra Madre Piedemont	0.13	0.94	0.17	0.85
ER-SP	ER-BT	Western Cordillera	0.20	0.92	-	-
ER-PK	ER-BT	Western Cordillera	0.24	0.90	-	-
<del>US-NR1</del>	<del>ER-BT</del>	<del>Western Cordillera</del>	<del>0.23</del>	<del>0.90</del>		

Formatted Table





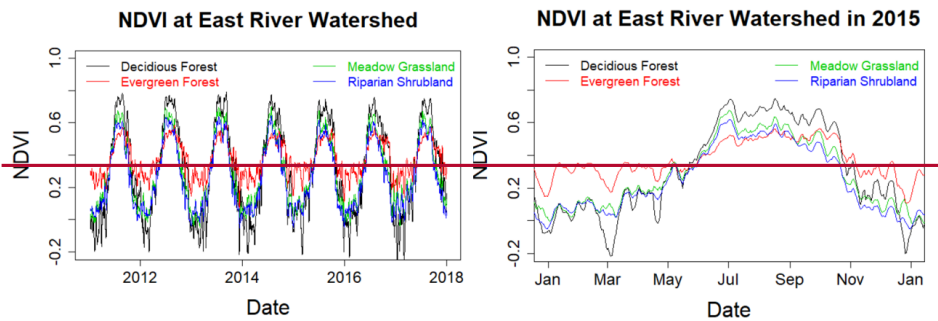
562  
 563 **Figure 97.** HPMs trained with CLM simulation at ER-BT are used to estimate ET at ER-SP, **ER-PK**, and **US-NR1**. Panels (a), (c), and (e) display the time series of HPM estimation of ET (red lines), as well as independent CLM estimation at ER-SP, and ER-PK, and eddy covariance measurements at US-NR1 (black lines). Panels (b), (d), and (f) show the scatter plots of daily (blue) and monthly (red) ET at these three sites. Darker blue clouds represent greater density of data points.

568 **4.4 Exploration of How ET and  $R_{ECO}$  Varies with Meteorological forcings** Use Case 4: HPM approach  
 569 **improved our prediction capability and Vegetation Heterogeneity process understanding at the East River**  
 570 **Watershed**

571 ET and  $R_{ECO}$  estimated from the HPM model at the mountainous East River Watershed in CO enabled us to  
 572 analyze how vegetation heterogeneity and meteorological forcings heterogeneity influence estimated ET and  $R_{ECO}$   
 573 dynamics, and to identify limitations in the developed approach for estimating ET and  $R_{ECO}$  across mountainous and  
 574 heterogeneous watersheds.

575 NDVI time series data provide high resolution (30m scale) information about vegetation variability across  
 576 the East River Watershed. The spatial distribution of vegetation cover presented in Figure 2 (from Falco et al. 2019)  
 577 enables us to distinguish different patches of deciduous forests, evergreen forests, meadow grassland and riparian  
 578 shrublands and retrieve corresponding NDVI time series. NDVI time series is related with snowmelt processes,

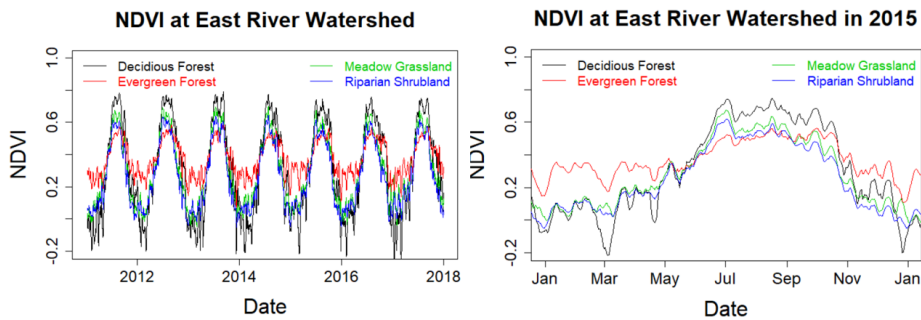
579 whereas earlier snowmelt triggers earlier vegetation growth and result in earlier rise NDVI values (Pedersen et al.,  
 580 2018). Figure 10 shows Landsat-derived and reconstructed NDVI values for the four different vegetation types within  
 581 the East River Watershed. March, April and May mean NDVI values in 2012 for site DF1 are 0.07, 0.22 and 0.37  
 582 respectively compared to 0.06, 0.15 and 0.33 in 2015. The early rise of NDVI values observed in April 2012 is  
 583 consistent with the fact that snowmelt occurred much earlier in 2012 than in 2015, as recorded by the SNOTEL Butte  
 584 station. Earlier increase of NDVI in earlier snowmelt year (2012) was also observed for other vegetation types. In  
 585 addition, evergreen forests have an extended growing season compared to the other vegetation types. For example,  
 586 March mean NDVI for EF1, RS1 and MS1 in 2012 are 0.30, 0.13, 0.11 compared to 0.28, 0.11, 0.08 in 2015,  
 587 respectively whereas May mean NDVI for EF1, RS1 and MS1 in 2012 are 0.38, 0.33, 0.35 compared to 0.34, 0.29  
 588 and 0.31 in 2015, respectively. Though earlier snowmelt triggers earlier increase in vegetation growth, significant  
 589 faster greenness was observed for deciduous forests, meadow grasslands and shrublands compared to evergreen forests,  
 590 where NDVI increased by 0.08, 0.20, 0.24 and 0.30 for evergreen forests, shrublands, grasslands and deciduous forests  
 591 in 2012, respectively. In addition, peak NDVI is generally smaller in evergreen forests compared to deciduous forests,  
 592 meadow grasslands and riparian shrublands. NDVI ranges from 0.2 to 0.6 for evergreen forests, whereas larger  
 593 fluctuations in NDVI are observed for deciduous forests, shrublands and grasslands. The NDVI values during the  
 594 winter are likely sensing both snow and forest density, due to pixel spatial averaging from Landsat images. Similar to  
 595 Qiao et al. (2016), we also found that the NDVI of deciduous forests exhibits a significant increase during the growing  
 596 season, followed by a sharp decline (likely caused by defoliation), and that evergreen forests had a more stable NDVI.  
 597 ~~Similar sharp decreases in the NDVI of riparian shrublands and meadow grasslands are observed.~~



598  
 599 **Figure 10** With the proposed HPM approach (e.g., mechanistic HPM), we were able to estimate ET and  $R_{eco}$   
 600 at selected locations at the East River Watershed, CO, USA with only meteorological forcings and remote sensing  
 601 data. Our estimations are comparable to other independent studies, such as Mu et al. (2013) (Fig. S2) and Berryman  
 602 et al. (2018). HPM estimations enhanced our understanding of watershed processes and enabled us to explore the  
 603 limitations in the developed HPM approach especially at mountainous watersheds.

604 Physiology differences among vegetation types and dynamic changes in meteorological conditions were well  
 605 captured by input features and HPM at the East River Watershed. Not surprisingly, the reconstructed NDVI indicated

606 that deciduous forests have the highest peak NDVI followed by grasslands, shrublands and evergreen forests whereas  
 607 annual variation of NDVI in evergreen forests is smaller than the other vegetation types (Fig. 8). Year 2012 is regarded  
 608 as a fore-summer drought year with earlier than normal snowmelt, and year 2015 is regarded as a normal water year.  
 609 The Palmer drought severity index (PDSI) is -5.2 and -1.5 for June and -4.6 and 1.1 for August in 2012 and 2015,  
 610 respectively. Dynamic changes in meteorological conditions between 2012 and 2015 were also reflected in the  
 611 reconstructed NDVI time series. We observed an earlier rise of NDVI in 2012: March, April and May mean NDVI  
 612 values for deciduous forest sites are 0.07, 0.2 and 0.37 compared to 0.06, 0.15 and 0.33 in 2015. Similar trends were  
 613 observed for other vegetation types during spring months as well. NDVI values remain high during the peak growing  
 614 season (deciduous forest > grassland > shrubland > evergreen forest) for both 2012 and 2015. However, we observed  
 615 NDVI declines for grasslands and shrublands since August in 2012 but not until September in 2015. During autumn  
 616 periods, NDVI declines significantly following the sharp decline in radiation.



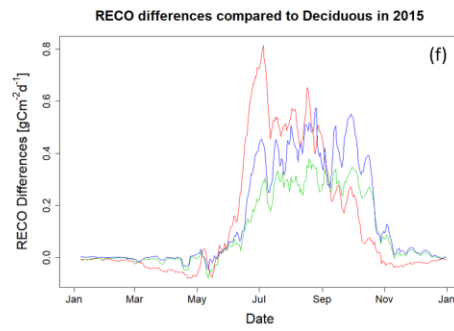
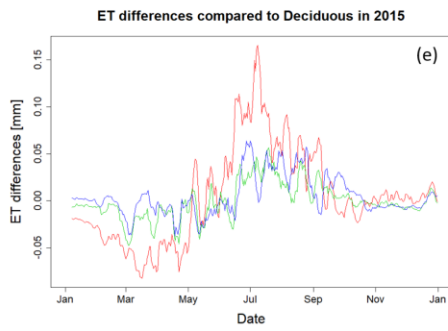
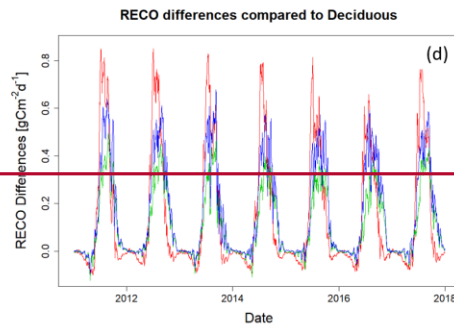
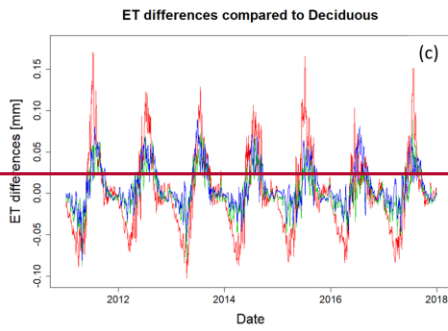
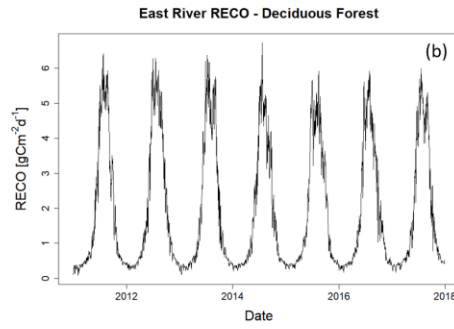
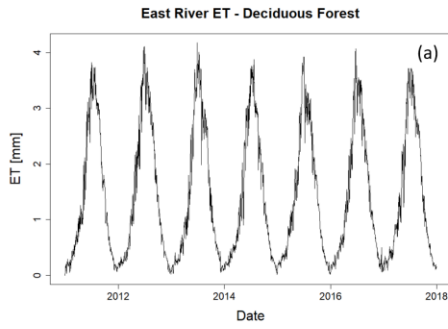
617  
 618 **Figure 8:** Reconstructed NDVI time series at selected locations in the East River Watershed for 2011 to 2018 (panel a) and  
 619 for 2015 (panel b, normal water year). Black, red, green, and blue lines represent the time series of NDVI for deciduous  
 620 forests, meadow grasslands, evergreen forests and riparian shrubland, respectively.

621 HPM-estimated ET and  $R_{ET}R_{eco}$  also show different dynamics with different vegetation types as a result of  
 622 differences in snowmelt timing and meteorological forcing and vegetation heterogeneity conditions. Figure 4a9a and  
 623 4b9b present the time series of estimated ET and  $R_{ET}R_{eco}$  associated with deciduous forests, respectively. Figure  
 624 4e9c and 4d9d present the ET and  $R_{ET}R_{eco}$  differences between deciduous forests sites and evergreen forests,  
 625 shrublands and grasslands. Before peak growing season, evergreen forests have the greatest ET and  $R_{ET}R_{eco}$   
 626 compared to the other vegetation types. ET of evergreen forests is about 10% greater than deciduous forests, whereas  
 627 ET of deciduous forests during peak growing season is greater than evergreen forests, shrublands and meadows. After  
 628 growing season, the NDVI of deciduous forests is less than 0.2 (loss of leaves) compared to the NDVI of evergreen  
 629 forests. Before peak growing season,  $R_{ET}R_{eco}$  of evergreen forests is slightly greater than deciduous forests, meadow  
 630 grasslands and shrublands. During peak growing season, we observed largest  $R_{ET}R_{eco}$  for deciduous forests sites (~  
 631  $6 \text{ gCm}^{-2}\text{d}^{-1}$ ) followed by meadows, shrublands and evergreen forests.  $R_{ET}R_{eco}$  of deciduous forests is around 17%  
 632 greater than  $R_{ET}R_{eco}$  of evergreen forests. However, we did not observe significant differences in annual ET among

633 these four vegetation types (e.g., DF+DF: 535 to 573 mm, MS+MS: 534 to 570 mm, RS+RS: 532 to 567 mm and  
634 EF+EF: 532 to 569 mm across 7 years in this study). Total annual  $R_{ETCO}$  of deciduous forests is greater than the  
635 other vegetation types (DF1: 642 to 698  $gCm^{-2}$ , MS1: 588 to 636  $gCm^{-2}$ , RS1: 589 to 636  $gCm^{-2}$  and EF1: 592 to  
636 639  $gCm^{-2}$ ). These results indicate HPM  $R_{eco}$  models are sensitive to vegetation types and HPM ET models are mostly  
637 constrained by meteorological conditions.

638 Considering the inter-annual variability in meteorological forcings, we further selected year 2014 (large snow  
639 precipitation ~ 587 mm but small rain precipitation ~ 275 mm) in addition to 2012 (drought year) and 2015 (small  
640 snow precipitation ~ 383 mm and large rain precipitation ~ 477 mm) to test HPM performance. As HPM does not  
641 have the capability to identify snow and monsoon precipitation's contribution to fluxes, we separated annual ET and  
642  $R_{eco}$  into pre-June (January-June) and post-July (July-December) to quantify the contribution from snow and monsoon.  
643 Earlier snowmelt that occurred in 2012 boosted spring ET and  $R_{eco}$  and we observed larger March-mean ET and  $R_{eco}$   
644 compared to 2014 and 2015 that are characterized by later snowmelt. Occurrences of fore-summer drought in 2012  
645 led to moisture limiting conditions, resulting in large fluctuations of ET and  $R_{eco}$  during May and June. ET fluctuated  
646 from 2.9 to 1.9  $mm d^{-1}$  during late May, and 3.53 to 2.6  $mm d^{-1}$  during early June. However, early occurrence of  
647 monsoon in 2012 led to a peak ET in early July. Due to late snowmelt, ET did not significantly fluctuate in 2014 and  
648 2015. However, peak ET shifted towards late July in 2014. Regarding  $R_{eco}$  dynamics, fore-summer drought conditions  
649 led to variations in  $R_{eco}$  from ~ 4 to 6  $gCm^{-2} d^{-1}$  in 2012. In 2014, we observed more steady increase of  $R_{eco}$  during  
650 the early and peak growing seasons. For late-summer and autumn months (August – October), ET decreased steadily  
651 in all three years regardless of monsoon precipitation inputs, following the significant decline in radiation. Pre-June  
652 ET and  $R_{eco}$  (255mm and 217  $gCm^{-2} d^{-1}$ ) were both greater in 2012 compared to 2014 (223 mm and  
653 178  $gCm^{-2} d^{-1}$ ) and 2015 (230 mm and 197  $gCm^{-2} d^{-1}$ ) in deciduous forests. While there were no significant  
654 differences in post-July ET among the three years (318, 316 and 306 mm), 2012 was the highest. Within deciduous  
655 forests and annually over 2012, 2014 and 2015, ET was 573 mm, 539 mm and 536 mm and  $R_{eco}$  was 698  $gCm^{-2}$ ,  
656 642  $gCm^{-2}$  and 652  $gCm^{-2}$ , respectively. Considering the inter-annual variability in snow dynamics, we observed  
657 annual ET at 569 mm and 532 mm and annual  $R_{ETCO}$  at 639  $gCm^{-2}$  and 602  $gCm^{-2}$  at EF1 for 2012 and 2015,  
658 respectively. We observed an earlier increase in ET and  $R_{ETCO}$  in 2012 with March mean ET and  $R_{ETCO}$  at 0.69  
659 mm/day and 0.51  $gCm^{-2} d^{-1}$  compared to 0.60 mm/day and 0.47  $gCm^{-2} d^{-1}$  in 2015. During peak growing  
660 season, we observed July mean ET at 3.43 and 3.33 mm/day and  $R_{ETCO}$  at 4.73 and 4.47  $gCm^{-2} d^{-1}$  for 2012  
661 and 2015, respectively. Though earlier snowmelt usually triggers summer drought conditions, we observed a  
662 significantly greater amount of monsoon precipitation in 2012 (3.06  $mm d^{-1}$ ) compared to 2015 (1.87  $mm d^{-1}$ ). Water  
663 stress situation caused by earlier snowmelt was largely compensated by earlier monsoon in 2012, and thus we observed  
664 higher March, July and annual ET and  $R_{ETCO}$  compared to 2015. Similar trends have also been observed for deciduous  
665 forests, shrublands and meadows in 2012 and 2015.

Formatted: Font: 10 pt, Not Bold

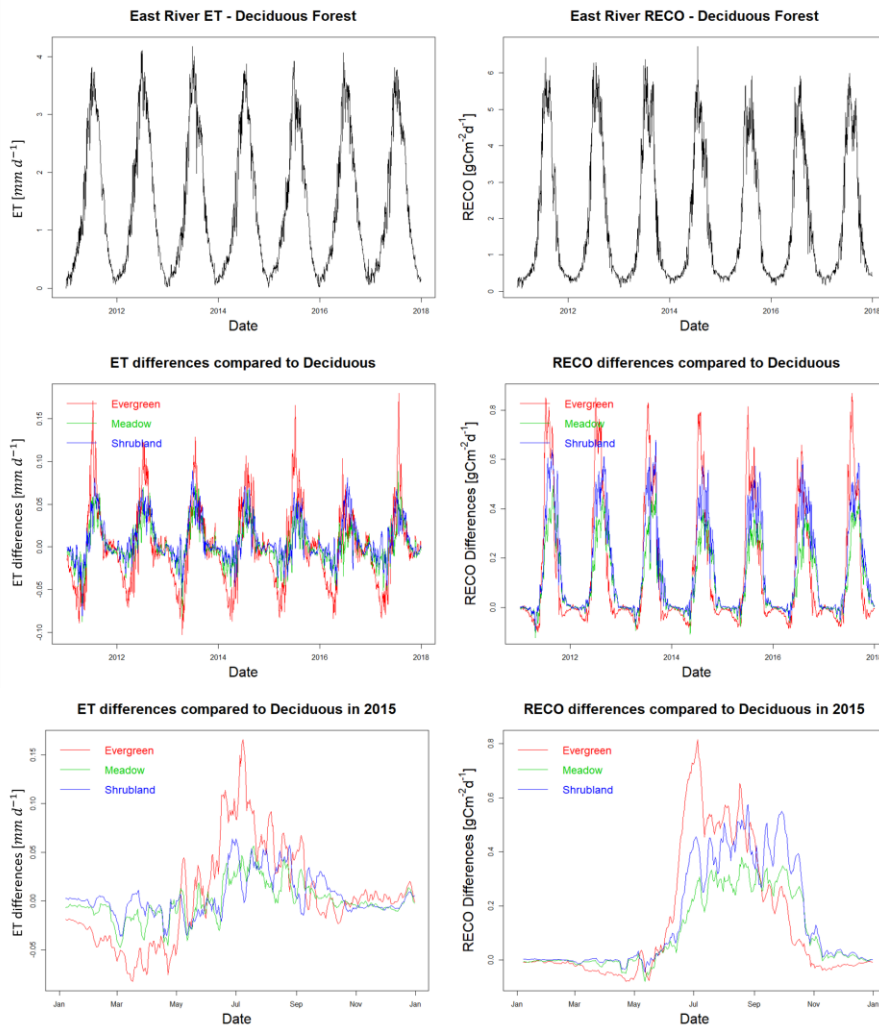


666

667

. Similar trends were observed for other vegetation types.





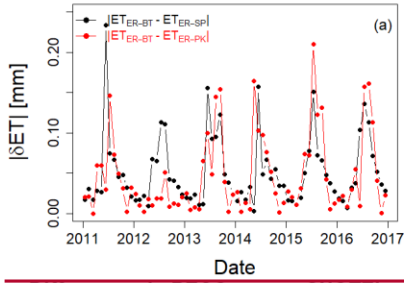
668

669 **Figure 49:** ET (a) and  $R_{ETCO}R_{eco}$  (b) estimation for the deciduous forest site DF1 at the East River Watershed. Panels (c)  
 670 and (d) show the differences in ET and  $R_{ETCO}R_{eco}$  among various vegetation types and **DF1-deciduous forest**. Red, green,  
 671 and blue lines represent the differences in evergreen forest, meadow, and riparian shrubland compared to **DF1-deciduous**  
 672 **forest**. Panels (e) and (f) zoom into 2015 to better display seasonal variations.

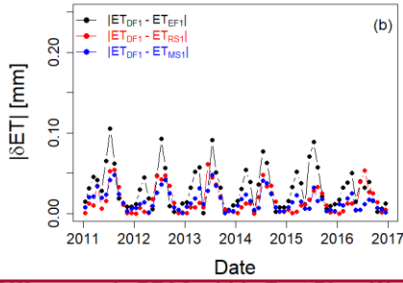
673 ET and  $R_{ETCO}$  estimation at the East River Watershed from the HPM model further enabled Though HPM  
 674 estimations allowed us to assess the role of input attributes and explore differences in ET and  $R_{eco}$  across vegetation  
 675 types and meteorological forcings heterogeneity, it is necessary to investigate the limitations of the HPM approach.

676 Figure 4210 shows the absolute value of monthly mean difference in ET (Fig. 42a10a and Fig. 42b10b) and  $R_{ETCO}R_{eco}$   
677 (Fig. 42e10c and Fig. 42d10d) across SNOTEL stations (ER-BT, ER-SP and ER-PK) and within selected East River  
678 locations. Landsat data enabled us to capture NDVI differences at these sites (Figure 10), but we have identified the  
679 insufficient resolution of input meteorological forcing data at the East River sites. We observed a We observed greater  
680 differences in air temperature and radiation at the SNOTEL sites whereas there's and very small differences at the East  
681 River sites (Figure S3). Summer S4. June air temperature differences among SNOTEL sites can be were occasionally  
682 over 3 °C but there's a barely 0.2 °C differences in, while the DAYMET data used for from the East River sites rarely  
683 revealed 0.2 °C differences. In addition, a  $\sim 80 W m^{-2} m^{-2}$  of radiation differences is was observed with SNOTEL data  
684 whereas radiation differences stays around  $30 W m^{-2} m^{-2}$  for East River sites. Correspondingly, we observed 2.5  
685 times greater differences in ET across SNOTEL stations compared to the sites within the East River watershed. We  
686 observed similar level of differences (around  $0.8 g C m^{-2}$ ) in  $R_{ETCO}R_{eco}$  within East River Watershed and across  
687 SNOTEL stations. Landsat data enabled us to capture NDVI differences at these sites, but we have identified the  
688 insufficient resolution of input meteorological forcing data at the East River sites. These results indicate uncertainties  
689 in meteorological forcing attributes (e.g., radiation and air temperature) can have a huge influence over HPM ET  
690 estimation and HPM  $R_{eco}$  model is more sensitive to temperature and radiation inputs whereas NDVI, temperature and  
691 radiation are all influential for HPM  $R_{ETCO}$  models. Differences in ET and  $R_{ETCO}$  among SNOTEL sites and East River  
692 sites are resulted from the differences in input meteorological forcing data NDVI datasets. If high resolution  
693 meteorological data becomes available for the East River watershed, we believe the HPM approach can better capture  
694 heterogeneities in ET and  $R_{ETCO}R_{eco}$  at the East River watershed and better distinguish the roles of meteorological  
695 forcing and vegetation heterogeneity on ET and  $R_{ETCO}R_{eco}$  distribution.

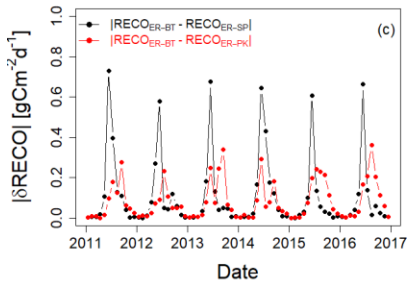
Differences in ET across SNOTEL sites



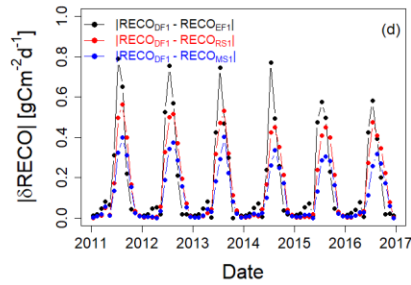
Differences in ET within East River Watershed



Differences in RECO across SNOTEL sites

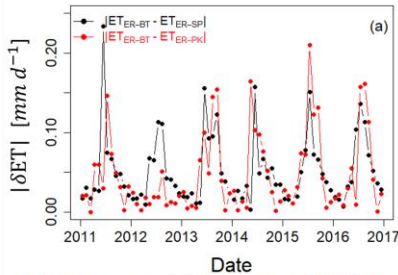


Differences in RECO within East River Watershed

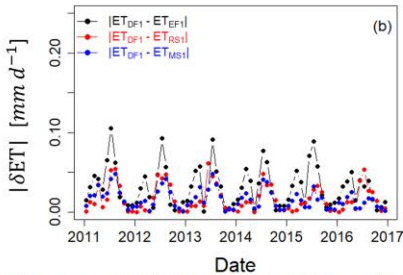


696

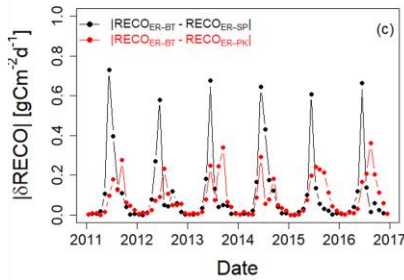
Differences in ET across SNOTEL sites



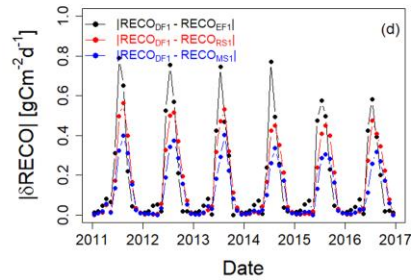
Differences in ET within East River Watershed



Differences in RECO across SNOTEL sites



Differences in RECO within East River Watershed



697

698 **Figure 4210.** Absolute differences in monthly mean ET and  $R_{ETCO}R_{eco}$  across SNOTEL stations and within East River  
699 Watershed. Panels (a) and (c) describe the absolute differences in monthly mean ET and  $R_{ETCO}R_{eco}$  between ER-BT, ER-SP,  
700 and ER-PK. Panels (b) and (d) describe the absolute differences in monthly mean ET and  $R_{ETCO}R_{eco}$  within East River  
701 Watershed between deciduous forest (DF1), forests, evergreen forest (EF1), forests, meadow (MS1), grasslands, and riparian  
702 shrubland (RS1), shrublands.

## 703 5. Discussion

704 Our study demonstrates that HPM provides reliable estimations of ET and  $R_{ETCO}R_{eco}$  under various climate  
705 and vegetation conditions, including data based HPMs that are trained with FLUXNET data as well as physical-  
706 model based HPMs that are coupled with simulations results. The unique gated structures and cell states of LSTM  
707 allow HPM to track information from mechanistic models (i.e., CLM in this study). With earlier times and decide  
708 which information to pass along and which information to forget. This effective configuration allows LSTM to  
709 effectively capture the long-term dependencies and ecological memory effects among meteorological forcings, NDVI,  
710 ET and  $R_{eco}$ . With 70 % of the data used for training (model development), ET and  $R_{ETCO}R_{eco}$  estimation from HPM  
711 achieves an average adjusted  $R^2$  of 0.9 compared to eddy covariance flux tower measurements. With this high  
712 estimation accuracy, we demonstrated that this approach could be used to demonstrate HPM's applicability for  
713 predicting ET and  $R_{ETCO}$  over time. HPM is capable of "learning" the complex interactions among meteorological  
714 forcings, vegetation dynamics, and water and carbon fluxes. The underlying relationships acquired by HPM can serve  
715 as a local ecohydrological model for long term monitoring of ET and  $R_{ETCO}$  with the aid of remote sensing data, and  
716 can fill in gap data during occasional equipment failure. HPM was also successful at estimating the spatial distribution  
717 of providing ET and  $R_{ETCO}$  through exploiting an ecoregion concept. Using the representative FLUXNET sites in  
718 different ecoregions, HPM provided estimates of  $R_{eco}$  estimation at sparsely monitored watersheds, we presented four  
719 use cases, including prediction ET and  $R_{ETCO}$  at locations using learned relationships  $R_{eco}$  in the time domain, data-  
720 driven HPMs and mechanistic HPMs. Results from other sites having the same ecoregion classification. For conditions  
721 where no FLUXNET sites are within the same ecoregion, our study showed that physically based models that utilize  
722 weather forcings data can provide alternatives for developing mechanistic HPM to the four use cases suggest HPM is  
723 a powerful approach to estimate ET and  $R_{ETCO}$ .

724 With the proposed HPM approach, we investigated the variability in ET and  $R_{ETCO}$  estimations across  
725 different proportions of the East River Watersheds. While we currently do not have continuous measurements of ET  
726  $R_{eco}$  at target watersheds requiring only 5 commonly available input data and  $R_{ETCO}$  at the East River Watershed for  
727 validation, our results are comparable to other studies that focus on sites within the same ecoregion. HPM based ET  
728 estimation at East River Watershed is comparable to Mu et al. (2013), where ET is computed based upon the logic of  
729 the Penman-Monteith equation and MODIS remote sensing data (Figure S1), and the HPM based  $R_{ETCO}$  estimation is  
730 comparable to what Berryman et al. (2018) discovered, with growing season  $R_{ETCO}$  ranging between 555 to 607  $gCm^{-2}$   
731 and mean growing season  $R_{ETCO}$  ranging between 3.01 to 3.30  $gCm^{-2}$ . Annual ET between deciduous forests and  
732 evergreen forests are not statistically different, which is similar to Mu et al. (2013). Annual  $R_{ETCO}$  differences between

733 evergreen forests and deciduous forests are around  $50 \text{ gCm}^{-2}$ , which is comparable to Berryman et al. 2018, can  
734 advance our understanding of watershed processes.

735 We confirmed the important role of vegetation heterogeneity in modeling ET and  $R_{\text{ECO}}$  dynamics, which  
736 further enabled us to better understand ecosystem dynamics at the East River Watershed. As indicated HPM was  
737 capable incorporating information from NDVI time series (Fig 10), to delineate the physiological differences among  
738 deciduous forests, evergreen forests, shrublands and grasslands. In our study, NDVI data indicated evergreen forests  
739 have a longer growing season compared to other vegetation types; however, and deciduous forests have higher peak  
740 NDVI values. Correspondingly, we also observed an earlier increase in ET and  $R_{\text{ECO}}$  for evergreen forests (before  
741 May), but larger ET and  $R_{\text{ECO}}$  for deciduous forests during peak growing season (around June and July). Similar  
742 dynamics were also observed at regions that have different climate conditions. Through assessing the differential  
743 mechanisms of deciduous forests and evergreen forests at various sites under Mediterranean climates, Baldocchi et al.  
744 (2010) found that deciduous forests had a shorter growing season, but showed a greater capacity for assimilating  
745 carbon during the growing season. Evergreen forests, on the other hand, had an extended growing season but with a  
746 smaller capacity for gaining carbon. These results were identified through analyzing the relationships among leaf ages,  
747 leaf nitrogen level, leaf area, and water use efficiencies of these tree species at the selected Mediterranean sites. They  
748 found older leaves tend to have smaller leaf nitrogen and stomata conductance that lead to smaller ET and  $R_{\text{ECO}}$   
749 during peak growing seasons. Though our approach were not able to quantify the physiology differences among  
750 vegetation types, HPM estimation indicated evergreen forests that maintain leaves throughout the year have smaller  
751 ET and  $R_{\text{ECO}}$  during peak growing season compared to other vegetation types.

752 Dynamic changes in the inter-annual variability of meteorological conditions result in varying growing  
753 season length and spatiotemporal variability in ET and  $R_{\text{ECO}}$ . Earlier snowmelt triggers earlier growth of vegetation,  
754 causing earlier rise in ET and  $R_{\text{ECO}}$ . However, earlier growth in vegetation and increasing demand for water results in  
755 drought conditions (Sloat et al., 2015; Wainwright et al., 2020) that decrease ET and  $R_{\text{ECO}}$ . Timing and amount of  
756 monsoon precipitation are also important monsoons can relieve water stress and lead to increases in ET and  $R_{\text{ECO}}$ .  
757 Combination of these events jointly determine the magnitude of annual ET and  $R_{\text{ECO}}$ . Hu et al. (2010) analyzed flux  
758 data at US-NRI to determine the relationships between growing season lengths and carbon sequestration, and found  
759 that extended growing season length resulted in less annual  $\text{CO}_2$  uptake. They found that the duration of growing  
760 seasons substantially decreases snow water storage, which significantly decreases forest carbon uptake. Wieder et al.  
761 (2017) used point-scale CLM to better understand how complex terrain controls landscape level variation of water,  
762 carbon and energy fluxes in the Niwot Ridge mountain ecosystems. With synthetic scenarios (e.g., different snow  
763 accumulation dynamics, fluctuations in air temperature), their simulation indicated earlier snowmelt and warmer  
764 summertime temperatures might drive divergent plant responses across the landscape. In our study, the combination  
765 of early snowmelt and early vegetation growth resulted in higher March ET and  $R_{\text{ECO}}$  in 2012 compared to 2015. The  
766 earlier start of growing season led to occurrences of fore-summer drought that decreases ET and  $R_{\text{ECO}}$ . However, the  
767 substantial earlier monsoon precipitation in 2012 relieved subsurface water stress whereas we observed higher July  
768 ET and  $R_{\text{ECO}}$  compared to other years. In addition, we observed smaller annual ET and  $R_{\text{ECO}}$  for evergreen forests

769 that have longer growing season compared to other vegetation types. These results suggested HPM is capable of  
770 translating these variabilities in meteorological forcing and vegetation variables to ET and  $R_{eco}$  dynamics. found that  
771 extended growing season length resulted in less annual  $CO_2$  uptake at Niwot Ridge, USA. They found increasing  
772 growing season length is usually correlated with decreasing snow water storage and decreasing forest carbon uptake.  
773 Xu et al. (2020) suggested canopy photosynthetic capacity is the driving force that lead to different resources use  
774 efficiencies (RUEs) between deciduous forests and evergreen forests. Novick et al. (2015) focused on the net  
775 ecosystem exchange of  $CO_2$  and also suggested seasonality is less important for evergreen forests, where significant  
776 amounts of carbon were assimilated outside of active season. These findings are similar to what we found in HPM  
777 estimations, where we observed a greater ET and  $R_{eco}$  contribution during early and later seasons for evergreen forests  
778 compared to deciduous forests that have significantly greater peak ET and  $R_{eco}$  during peak growing season. As HPM  
779 only requires 5 input features and NDVI is the only variable related with vegetation types, we were not able to perform  
780 detailed analysis delineating the physiological control on ET and  $R_{eco}$  dynamics. But we believe HPM models are still  
781 useful as they can provide initial ET and  $R_{eco}$  estimation that help with site selection and field campaign designs.

782 Through comparing the HPM estimation results at different ecoregions, we also identified and assessed the  
783 limitations of current selection of input parameters. In the current study, we only used meteorological forcing and  
784 remote sensing based variables as inputs for HPM models, because these data are generally acquirable from weather  
785 reanalysis datasets and remote sensing products. HPM models with these variables provided reasonable estimates of  
786 ET and  $R_{eco}$  for ecoregions limited by energy conditions, however we observed a decreasing prediction accuracy for  
787 ecoregions that experience seasonally dry periods. For example, HPM estimates at US-NRI and CA-OAS achieved  
788 very high  $R^2$  and small MAE; but prediction accuracy decreases especially during peak growing season at US-Ton  
789 and other water limiting sites. These results indicate other key variables are necessary in order to capture dynamics  
790 during the seasonally dry periods, such as soil moisture measurement. The current HPM models did not use soil  
791 moisture as an input variable due to data availability reasons, but we believe and recommend adding soil moisture as  
792 well as other key variables to HPMS to further improve model performance at these seasonally dry ecoregions when  
793 such data becomes available.

794 Parameterization and spatiotemporal resolution of meteorological forcing data still remain a challenge for  
795 improving ET and  $R_{eco}$  estimation at sparsely monitored watersheds. Microclimate and heterogeneities in  
796 meteorological forcing attributes control the magnitude and timing of ET and  $R_{eco}$  dynamics. Other field temporal  
797 variability in meteorological conditions also leads to unique ET and  $R_{eco}$  responses at the East River Watershed, as  
798 shown by HPM estimations. Three years with a diverse combination of snow and rain precipitation were analyzed. In  
799 2012, a year that experienced earlier snowmelt, both ET and  $R_{eco}$  increased early in the season. However, earlier  
800 growth in vegetation and increasing demand for water resulted in fore-summer drought conditions that led to decreases  
801 in ET and  $R_{eco}$  in late May and June. In 2014, HPM estimated a steady increase in ET and  $R_{eco}$  during spring months  
802 following radiation and air temperature trends, with no subsequent significant decline in ET and  $R_{eco}$ . This indicates  
803 that energy was still the key limiting factor for spring dynamics in 2014, leading to a smaller pre-June ET and  $R_{eco}$   
804 compared to 2012. Following an earlier arrival of monsoon in 2012 compared to 2014 and 2015, we observed higher

805 mean ET and  $R_{eco}$  in July than in June, which indicates the earlier arrival of monsoon precipitation greatly reduced the  
806 moisture limiting condition caused by fore-summer drought and led to subsequent increase in ET and  $R_{eco}$ . During late  
807 summer and autumn months, radiation declined significantly with ~ 30 % decrease in August and ~ 40 % decrease in  
808 September. Though 2012, 2014 and 2015 had diverse monsoon precipitation during these periods, HPM did not  
809 estimate significant differences in post-July ET. This result indicates the East River watershed is mainly under energy-  
810 limiting rather than moisture-limiting conditions during late-summer and autumn; and timing of monsoon arrival is  
811 more important than the absolute amount of monsoon precipitation for ET dynamics. This result is consistent with  
812 findings in Carroll et al. (2020). Their study also indicated earlier arrival of summer monsoon was effectively  
813 supporting ET and that the monsoon precipitation was quickly consumed by vegetation, whereas later arrival of  
814 summer monsoon water mainly contributed to streamflow under energy-limiting conditions.

815 Uncertainties of HPM models arise from several aspects. First, current choices of only five input features  
816 based on data availability may decrease estimation accuracy in certain environments, such as sites with seasonally dry  
817 periods. Though the LSTM component within HPMs can capture the memory effects and long-term dependencies of  
818 watershed dynamics, rare extreme values are difficult to be captured by LSTM due to insufficient training data for  
819 such cases. For example, we observed a decreasing prediction accuracy for ET and  $R_{eco}$  estimation at sites that  
820 experience drought conditions. Current use of meteorological forcings data and NDVI may not provide sufficient data  
821 for LSTM to identify droughts implicitly. Other key variables (e.g., soil moisture) when available can potentially be  
822 useful to help LSTM better quantify these rare events and increase model performance. Secondly, parameterization  
823 and insufficient spatiotemporal resolution of meteorological data still remain a challenge. Field observations along the  
824 Rocky Mountain ranges have shown that south-facing hillslopes have significantly earlier snowmelt compared to  
825 north-facing hillslopes (Kampf et al., 2015; Webb et al., 2018), which are hypothesized to result in significant  
826 differences in ET and  $R_{eco}$  dynamics. We compared ET and  $R_{eco}$  differences among SNOTEL sites and East River  
827 sites and identified ET differences among SNOTEL sites are greater than the differences among East River sites but  
828  $R_{eco}$  differences are similar between the two groups. Data from weather stations (SNOTEL sites) captured the  
829 spatiotemporal heterogeneity in radiation and temperature, however DAYMET data suggested very small differences  
830 in radiation and temperature (Figure S3 and S4). The insufficient spatial resolution of input meteorological forcing  
831 data limits HPM performance at the East River Watershed. Uncertainties in meteorological inputs can result in large  
832 errors (i.e., >20% MAE) and reduce accuracy by 10–30% in ET and  $R_{eco}$  estimations as suggested by. However, we  
833 did not observe same level of heterogeneities in radiation and air temperature in reanalysis data compared to weather  
834 station data (Fig. S4 and S5). Mu et al. (2013) and Zhang et al. (2019). Thus, there is still a significant need for high-  
835 spatial-resolution suggested uncertainties in meteorological forcing data products to enable better estimates of ET  
836 inputs can result in large errors (i.e., > 20 % MAE) and  $R_{eco}$  and assess the governing factors that regulate their  
837 spatiotemporal variability.

838 In addition to the quality of meteorological data reduce accuracy by 10 – 30 %. Additionally, HPM is also  
839 influenced by remote sensing inputs accuracy. Incorrectly calculated or pixel-averaged NDVI values from Landsat  
840 images can greatly alter HPM outputs for ET and  $R_{eco}$ . Satellite images with different, including but not limited to

841 ~~insufficient resolution, cloud cover have a slight influence over the NDVI values calculated, which do not represent~~  
842 ~~real-time vegetation conditions. Algorithms used to reconstruct daily NDVI time series are also subject to uncertainties,~~  
843 ~~spatial averaging, temporal reconstruction, any other algorithms involved.~~ But with recent advances in remote sensing  
844 and satellite technologies (McCabe et al., 2017) and harmonized Landsat-Sentinel datasets (Claverie et al., 2018), the  
845 spatial and temporal resolution should greatly increase in the future (i.e., 3 m resolution and daily). ~~These advances~~  
846 ~~will lead to more accurate classification of vegetation types and NDVI calculations, which are expected to decrease~~  
847 ~~uncertainty associated with flux estimation.~~ Finally, errors can stem from the HPM hybrid approaches and conceptual  
848 ~~model uncertainties. Any original errors in mechanistic models will be passed onto HPM estimations of ET and  $R_{eco}$ .~~  
849 ~~We recommend to train data-driven HPM and mechanistic HPM using long time series (e.g., > 5 years) with high~~  
850 ~~quality data or simulations, which enables HPMs to better memorize long-term dependencies of ecosystem dynamics.~~  
851 ~~Though some of the uncertainties still remain a challenge, efforts have been made to minimize them through the~~  
852 ~~technical advances described herein. Future HPM models can potentially be jointly trained on FLUXNET and process-~~  
853 ~~based simulations to bypass certain limitations and provide more accurate ET and  $R_{eco}$  at sparsely monitored~~  
854 ~~watersheds.~~

855 ~~Another source of uncertainty in HPM arises from the choice of hybrid approaches and any parameter~~  
856 ~~uncertainties in mechanistic models. Since HPM relies on accurate ET and  $R_{eco}$  inputs from flux towers or~~  
857 ~~mechanistic models, any uncertainties in measuring or modeling ET and  $R_{eco}$  will propagate to HPM. If HPM is~~  
858 ~~developed with a mechanistic model that has such missing components, these biases will be passed on to HPM~~  
859 ~~estimation of ET and  $R_{eco}$ . Parameter and conceptual model uncertainties in mechanistic models also restrict HPM's~~  
860 ~~ability to "learn" the ecosystem dynamics. In order to reduce potential biasedness, we trained data-based HPM and~~  
861 ~~physical model-based HPM upon long time series (e.g., > 5 years) with quality assessed data or simulation results,~~  
862 ~~which also enables HPM to better memorize long time dependencies of ecosystem dynamics. Though the~~  
863 ~~quantification of uncertainties remains challenging, efforts have been made to lower these uncertainties using the~~  
864 ~~technical advances described here.~~

## 865 6. Conclusion

866 In this study, we developed and tested a Hybrid Predictive Modeling (HPM) approach for ET and  $R_{eco}$   
867 estimation, with ~~an enhanced~~ focus on ~~mountainous watersheds~~ a watershed in the Rocky Mountains. We developed  
868 individual HPM models at various FLUXNET sites and at sites where data ~~can support~~ could support the proper  
869 development of a mechanistic model (e.g., CLM). These models were validated against eddy covariance  
870 measurements and CLM outputs. We further used these models for ET and  $R_{eco}$  estimation at watersheds within  
871 the same ecoregion to test HPM's capability of providing estimation over space, where only meteorological forcings  
872 data and remote sensing data were available. Lastly, we applied the HPM to provide long-term estimation of ET and  
873  $R_{eco}$  and test the sensitivity of HPM to various vegetation ~~types at various sites~~ and meteorological conditions  
874 within the East River Watershed of CO, USA.

Formatted: Subscript



875 Given the promising results of HPM, ~~this work~~the approach offers an avenue for estimating ET and  $R_{eco}$ .  
876 using easy-to-acquire or commonly available datasets. This study also suggests that the spatial heterogeneity of  
877 meteorological forcings and vegetation dynamics have significant impacts on ET and  $R_{eco}$  dynamics, which may  
878 be currently underestimated due to typically coarse spatial resolution of data inputs. Parameters related to energy and  
879 soil moisture conditions can be implemented into HPM to increase HPM's accuracy, especially for sites in ecoregions  
880 limited by soil moisture conditions. Lastly, it should be pointed out that HPM is not restricted to estimation of ET and  
881  $R_{eco}$  only. ~~We focused here on developing HPM for ET and  $R_{eco}$ , but~~ $R_{eco}$  only. HPM also has great potential for  
882 estimating other parameters important for water and carbon cycles given the right choice of input variables. ~~Indeed,~~  
883 ~~other attributes~~, such as net ecosystem exchange (Figure A6). Thus, we believe the proposed HPM model can improve  
884 our prediction capabilities of ET and sensible heat flux, might also be accurately captured $R_{eco}$  at sparsely monitored  
885 watersheds and represented with HPM, given the right choice of featuresadvance our understanding of watershed  
886 dynamics.

887 **Data availability.** The data used in this study are from publicly available datasets. FLUXNET measurements can be  
888 accessed at <https://FLUXNET.fluxdata.org>. SNOTEL data are available at <https://www.wcc.nrcs.usda.gov/snow/>.  
889 DAYMET data can be found at (Thornton et al., 2017) or via Google Earth Engine. Landsat data are available on  
890 Google Earth Engine. All data and simulated results and model parameters associated with this article can be found at  
891 <https://data.ess-dive.lbl.gov/view/doi:10.15485/1633810>.

892 **Acknowledgement.** Acknowledgements. This material is based upon work supported as part of the Watershed  
893 Function Scientific Focus Area funded by the U.S. Department of Energy, Office of Science, Office of Biological and  
894 Environmental Research under Award Number DE-AC02-05CH11231. We thank Haruko Wainwright and Bhavna  
895 Arora for providing comments on East River estimations. We also greatly appreciate all the guidance provided by  
896 Professor Yoram Rubin and Professor Dennis Baldocchi at UC Berkeley to the first author. We also acknowledge the  
897 Jane Lewis Fellowship Committee of the UC Berkeley for providing fellowship support to the first author.

## 898 References

- 899 Abatzoglou, J. T., Barbero, R., Wolf, J. W. and Holden, Z. A.: Tracking Interannual Streamflow Variability with  
900 Drought Indices in the U.S. Pacific Northwest, J. Hydrometeorol., doi:10.1175/jhm-d-13-0167.1, 2014.
- 901 Ai, J., Jia, G., Epstein, H. E., Wang, H., Zhang, A. and Hu, Y.: MODIS-Based Estimates of Global Terrestrial  
902 Ecosystem Respiration, J. Geophys. Res. Biogeosciences, 123(2), 326–352, doi:10.1002/2017JG004107, 2018.
- 903 Allen, R. G., Pereira, L. S., Raes, D. and Smith, M.: Crop evapotranspiration: Guidelines for computing crop  
904 requirements., 1998.
- 905 Anderson, M. C., Allen, R. G., Morse, A. and Kustas, W. P.: Use of Landsat thermal imagery in monitoring  
906 evapotranspiration and managing water resources, Remote Sens. Environ., doi:10.1016/j.rse.2011.08.025, 2012.
- 907 Baldocchi, D.: Measuring fluxes of trace gases and energy between ecosystems and the atmosphere - the state and  
908 future of the eddy covariance method, Glob. Chang. Biol., doi:10.1111/gcb.12649, 2014.
- 909 Baldocchi, D. D., Ma, S., Rambal, S., Misson, L., Ourcival, J. M., Limousin, J. M., Pereira, J. and Papale, D.: On the  
910 differential advantages of evergreenness and deciduousness in mediterranean oak woodlands: A flux perspective,  
911 Ecol. Appl., 20(6), 1583–1597, doi:10.1890/08-2047.1, 2010.

912 Berryman, E. M., Vanderhoof, M. K., Bradford, J. B., Hawbaker, T. J., Henne, P. D., Burns, S. P., Frank, J. M.,  
913 Birdsey, R. A. and Ryan, M. G.: Estimating Soil Respiration in a Subalpine Landscape Using Point, Terrain,  
914 Climate, and Greenness Data, *J. Geophys. Res. Biogeosciences*, 123(10), 3231–3249, doi:10.1029/2018JG004613,  
915 2018.

916 Bodesheim, P., Jung, M., Gans, F., Mahecha, M. D. and Reichstein, M.: Upscaled diurnal cycles of land-  
917 Atmosphere fluxes: A new global half-hourly data product, *Earth Syst. Sci. Data*, 10(3), 1327–1365,  
918 doi:10.5194/essd-10-1327-2018, 2018.

919 [De Bruin, H. A. R.: A model for the Priestley-Taylor parameter alpha., \*J. Clim. Appl. Meteorol.\*, doi:10.1175/1520-](#)  
920 [0450\(1983\)0222-0.CO;2, 1983.](#)

921 Budyko, M. I.: The Heat Balance of the Earth's Surface, *Sov. Geogr.*, 2(4), 3–13,  
922 doi:10.1080/00385417.1961.10770761, 1961.

923 [Carroll, R. W. H., Gochis, D. and Williams, K. H.: Efficiency of the Summer Monsoon in Generating Streamflow](#)  
924 [Within a Snow-Dominated Headwater Basin of the Colorado River, \*Geophys. Res. Lett.\*, 47\(23\),](#)  
925 [doi:10.1029/2020GL090856, 2020.](#)

926 Chang, L. L., Dwivedi, R., Knowles, J. F., Fang, Y. H., Niu, G. Y., Pelletier, J. D., Rasmussen, C., Durcik, M.,  
927 Barron-Gafford, G. A. and Meixner, T.: Why Do Large-Scale Land Surface Models Produce a Low Ratio of  
928 Transpiration to Evapotranspiration?, *J. Geophys. Res. Atmos.*, doi:10.1029/2018JD029159, 2018.

929 [Chu, H., Luo, X., Ouyang, Z., Chan, W. S., Dengel, S., Biraud, S. C., Torn, M. S., Metzger, S., Kumar, J., Arain, M.](#)  
930 [A., Arkebauer, T. J., Baldocchi, D., Bernacchi, C., Billesbach, D., Black, T. A., Blanken, P. D., Bohrer, G., Bracho,](#)  
931 [R., Brown, S., Brunzell, N. A., Chen, J., Chen, X., Clark, K., Desai, A. R., Duman, T., Durden, D., Fares, S.,](#)  
932 [Forbrich, I., Gamon, J. A., Gough, C. M., Griffis, T., Helbig, M., Hollinger, D., Humphreys, E., Ikawa, H., Iwata,](#)  
933 [H., Ju, Y., Knowles, J. F., Knox, S. H., Kobayashi, H., Kolb, T., Law, B., Lee, X., Litvak, M., Liu, H., Munger, J.](#)  
934 [W., Noormets, A., Novick, K., Oberbauer, S. F., Oechel, W., Oikawa, P., Papuga, S. A., Pendall, E., Prajapati, P.,](#)  
935 [Prueger, J., Quinton, W. L., Richardson, A. D., Russell, E. S., Scott, R. L., Starr, G., Staebler, R., Stoy, P. C., Stuart-](#)  
936 [Haëntjens, E., Sonnentag, O., Sullivan, R. C., Suyker, A., Ueyama, M., Vargas, R., Wood, J. D. and Zona, D.:](#)  
937 [Representativeness of Eddy-Covariance flux footprints for areas surrounding AmeriFlux sites, \*Agric. For. Meteorol.\*,](#)  
938 [301–302\(February\), doi:10.1016/j.agrformet.2021.108350, 2021.](#)

939 Claverie, M., Ju, J., Masek, J. G., Dungan, J. L., Vermote, E. F., Roger, J. C., Skakun, S. V. and Justice, C.: The  
940 Harmonized Landsat and Sentinel-2 surface reflectance data set, *Remote Sens. Environ.*,  
941 doi:10.1016/j.rse.2018.09.002, 2018.

942 Cox, P. M., Betts, R. A., Jones, C. D., Spall, S. A. and Totterdell, I. J.: Acceleration of global warming due to  
943 carbon-cycle feedbacks in a coupled climate model, *Nature*, doi:10.1038/35041539, 2000.

944 Dagers, T. D., Kromkamp, J. C., Herman, P. M. J. and van der Wal, D.: A model to assess microphytobenthic  
945 primary production in tidal systems using satellite remote sensing, *Remote Sens. Environ.*, 211(April), 129–145,  
946 doi:10.1016/j.rse.2018.03.037, 2018.

947 Falco, N., Wainwright, H., Dafflon, B., Léger, E., Peterson, J., Steltzer, H., Wilmer, C., Rowland, J. C., Williams, K.  
948 H. and Hubbard, S. S.: Investigating Microtopographic and Soil Controls on a Mountainous Meadow Plant  
949 Community Using High-Resolution Remote Sensing and Surface Geophysical Data, *J. Geophys. Res.*  
950 *Biogeosciences*, doi:10.1029/2018JG004394, 2019.

951 Gao, X., Mei, X., Gu, F., Hao, W., Li, H. and Gong, D.: Ecosystem respiration and its components in a rainfed  
952 spring maize cropland in the Loess Plateau, China, *Sci. Rep.*, doi:10.1038/s41598-017-17866-1, 2017.

953 Gao, Y., Yu, G., Li, S., Yan, H., Zhu, X., Wang, Q., Shi, P., Zhao, L., Li, Y., Zhang, F., Wang, Y. and Zhang, J.: A  
954 remote sensing model to estimate ecosystem respiration in Northern China and the Tibetan Plateau, *Ecol. Modell.*,  
955 doi:10.1016/j.ecolmodel.2015.03.001, 2015.

956 van Gorsel, E., Delpierre, N., Leuning, R., Black, A., Munger, J. W., Wofsy, S., Aubinet, M., Feigenwinter, C.,  
957 Beringer, J., Bonal, D., Chen, B., Chen, J., Clement, R., Davis, K. J., Desai, A. R., Dragoni, D., Etzold, S.,  
958 Grünwald, T., Gu, L., Heinesch, B., Hutryra, L. R., Jans, W. W. P., Kutsch, W., Law, B. E., Leclerc, M. Y.,

- 959 Mammarella, I., Montagnani, L., Noormets, A., Rebmann, C. and Wharton, S.: Estimating nocturnal ecosystem  
960 respiration from the vertical turbulent flux and change in storage of CO<sub>2</sub>, *Agric. For. Meteorol.*, 149(11), 1919–  
961 1930, doi:10.1016/j.agrformet.2009.06.020, 2009.
- 962 Greve, P., Gudmundsson, L., Orłowsky, B. and Seneviratne, S. I.: Introducing a probabilistic Budyko framework,  
963 *Geophys. Res. Lett.*, 42(7), 2261–2269, doi:10.1002/2015GL063449, 2015.
- 964 Hargrove, W. W. and Hoffman, F. M.: Using multivariate clustering to characterize ecoregion borders, *Comput. Sci.*  
965 *Eng.*, 1(4), 18–25, doi:10.1109/5992.774837, 1999.
- 966 Hargrove, W. W., Hoffman, F. M. and Law, B. E.: New analysis reveals representativeness of the amerflux network,  
967 *Eos (Washington, DC)*, 84(48), doi:10.1029/2003EO480001, 2003.
- 968 Hochreiter, S. and Schmidhuber, J.: Long Short-Term Memory, *Neural Comput.*, doi:10.1162/neco.1997.9.8.1735,  
969 1997.
- 970 Homer, C., Dewitz, J., Yang, L., Jin, S., Danielson, P., Xian, G., Coulston, J., Herold, N., Wickham, J. and Megown,  
971 K.: Completion of the 2011 national land cover database for the conterminous United States – Representing a  
972 decade of land cover change information, *Photogramm. Eng. Remote Sensing*, doi:10.1016/S0099-1112(15)30100-  
973 2, 2015.
- 974 Hu, J., Moore, D. J. P., Burns, S. P. and Monson, R.: Longer growing seasons lead to less carbon sequestration by a  
975 subalpine forest, *Glob. Chang. Biol.*, 16(2), 771–783, doi:10.1111/j.1365-2486.2009.01967.x, 2010.
- 976 Hubbard, S. S., Williams, K. H., Agarwal, D., Banfield, J., Beller, H., Bouskill, N., Brodie, E., Carroll, R., Dafflon,  
977 B., Dwivedi, D., Falco, N., Faybishenko, B., Maxwell, R., Nico, P., Steefel, C., Steltzer, H., Tokunaga, T., Tran, P.  
978 A., Wainwright, H. and Varadharajan, C.: The East River, Colorado, Watershed: A Mountainous Community  
979 Testbed for Improving Predictive Understanding of Multiscale Hydrological–Biogeochemical Dynamics, *Vadose*  
980 *Zo. J.*, 17(1), 0, doi:10.2136/vzj2018.03.0061, 2018.
- 981 IPCC: IPCC 2019- Special report on climate change, desertification, land degradation, sustainable land  
982 management, food security, and greenhouse gas fluxes in terrestrial ecosystem, *Res. Handb. Clim. Chang. Agric.*  
983 *Law*, doi:10.4337/9781784710644, 2019.
- 984 Irons, J. R., Dwyer, J. L. and Barsi, J. A.: The next Landsat satellite: The Landsat Data Continuity Mission, *Remote*  
985 *Sens. Environ.*, doi:10.1016/j.rse.2011.08.026, 2012.
- 986 Jägermeyr, J., Gerten, D., Lucht, W., Hostert, P., Migliavacca, M. and Nemani, R.: A high-resolution approach to  
987 estimating ecosystem respiration at continental scales using operational satellite data, *Glob. Chang. Biol.*,  
988 doi:10.1111/gcb.12443, 2014.
- 989 Jung, M., Reichstein, M., Ciais, P., Seneviratne, S. I., Sheffield, J., Goulden, M. L., Bonan, G., Cescatti, A., Chen,  
990 J., De Jeu, R., Dolman, A. J., Eugster, W., Gerten, D., Gianelle, D., Gobron, N., Heinke, J., Kimball, J., Law, B. E.,  
991 Montagnani, L., Mu, Q., Mueller, B., Oleson, K., Papale, D., Richardson, A. D., Rouspard, O., Running, S.,  
992 Tomelleri, E., Viovy, N., Weber, U., Williams, C., Wood, E., Zaehle, S. and Zhang, K.: Recent decline in the global  
993 land evapotranspiration trend due to limited moisture supply, *Nature*, doi:10.1038/nature09396, 2010.
- 994 Jung, M., Reichstein, M., Schwalm, C. R., Huntingford, C., Sitch, S., Ahlström, A., Armeth, A., Camps-Valls, G.,  
995 Ciais, P., Friedlingstein, P., Gans, F., Ichii, K., Jain, A. K., Kato, E., Papale, D., Poulter, B., Raduly, B., Rödenbeck,  
996 C., Tramontana, G., Viovy, N., Wang, Y. P., Weber, U., Zaehle, S. and Zeng, N.: Compensatory water effects link  
997 yearly global land CO<sub>2</sub> sink changes to temperature, *Nature*, 541(7638), 516–520, doi:10.1038/nature20780, 2017.
- 998 [Kakalia, Z., Varadharajan, C., Alper, E., Brodie, E., Burrus, M., Carroll, R., Christianson, D., Hendrix, V.,](https://doi.org/10.22541/au.160157556.64095872)  
999 [Henderson, M., Hubbard, S., Johnson, D., Versteeg, R., Williams, K. and Agarwal, D.: The East River Community](https://doi.org/10.22541/au.160157556.64095872)  
1000 [Observatory Data Collection: Diverse, multiscale data from a mountainous watershed in the East River, Colorado, .](https://doi.org/10.22541/au.160157556.64095872)  
1001 [1–17 \[online\] Available from: https://doi.org/10.22541/au.160157556.64095872, 2020.](https://doi.org/10.22541/au.160157556.64095872)
- 1002 Kampf, S., Markus, J., Heath, J. and Moore, C.: Snowmelt runoff and soil moisture dynamics on steep subalpine  
1003 hillslopes, *Hydrol. Process.*, 29(5), 712–723, doi:10.1002/hyp.10179, 2015.

1004 Keenan, T. F., Migliavacca, M., Papale, D., Baldocchi, D., Reichstein, M., Torn, M. and Wutzler, T.: Widespread  
1005 inhibition of daytime ecosystem respiration, *Nat. Ecol. Evol.*, 3(3), 407–415, doi:10.1038/s41559-019-0809-2, 2019.

1006 Knowles, J. F., Blanken, P. D. and Williams, M. W.: Wet meadow ecosystems contribute the majority of overwinter  
1007 soil respiration from snow-scoured alpine tundra, *J. Geophys. Res. G Biogeosciences*, 121(4), 1118–1130,  
1008 doi:10.1002/2015JG003081, 2016.

1009 Kratzert, F., Klotz, D., Brenner, C., Schulz, K. and Herrnegger, M.: Rainfall–runoff modelling using Long Short-  
1010 Term Memory (LSTM) networks, *Hydrol. Earth Syst. Sci.*, 22(11), 6005–6022, doi:10.5194/hess-22-6005-2018,  
1011 2018.

1012 Lasslop, G., Reichstein, M., Papale, D., Richardson, A., Arneeth, A., Barr, A., Stoy, P. and Wohlfahrt, G.: Separation  
1013 of net ecosystem exchange into assimilation and respiration using a light response curve approach: Critical issues  
1014 and global evaluation, *Glob. Chang. Biol.*, 16(1), 187–208, doi:10.1111/j.1365-2486.2009.02041.x, 2010.

1015 Livingston, G. P. and Hutchinson, G. L.: Enclosure-based measurement of trace gas exchange: applications and  
1016 sources of error., 1995.

1017 Ma, Y., Liu, S., Song, L., Xu, Z., Liu, Y., Xu, T. and Zhu, Z.: Estimation of daily evapotranspiration and irrigation  
1018 water efficiency at a Landsat-like scale for an arid irrigation area using multi-source remote sensing data, *Remote  
1019 Sens. Environ.*, 216(August), 715–734, doi:10.1016/j.rse.2018.07.019, 2018.

1020 Main-Knorn, M., Pflug, B., Louis, J., Debaecker, V., Müller-Wilm, U. and Gascon, F.: Sen2Cor for Sentinel-2.,  
1021 2017.

1022 McCabe, M. F., Aragon, B., Houborg, R. and Mascaro, J.: CubeSats in Hydrology: Ultrahigh-Resolution Insights  
1023 Into Vegetation Dynamics and Terrestrial Evaporation, *Water Resour. Res.*, 53(12), 10017–10024,  
1024 doi:10.1002/2017WR022240, 2017.

1025 Metzger, S., Junkermann, W., Mauder, M., Butterbach-Bahl, K., Trancón Y Widemann, B., Neidl, F., Schäfer, K.,  
1026 Wieneke, S., Zheng, X. H., Schmid, H. P. and Foken, T.: Spatially explicit regionalization of airborne flux  
1027 measurements using environmental response functions, *Biogeosciences*, 10(4), 2193–2217, doi:10.5194/bg-10-  
1028 2193-2013, 2013.

1029 Migliavacca, M., Reichstein, M., Richardson, A. D., Mahecha, M. D., Cremonese, E., Delpierre, N., Galvagno, M.,  
1030 Law, B. E., Wohlfahrt, G., Andrew Black, T., Carvalhais, N., Ceccherini, G., Chen, J., Gobron, N., Koffi, E.,  
1031 William Munger, J., Perez-Priego, O., Robustelli, M., Tomelleri, E. and Cescatti, A.: Influence of physiological  
1032 phenology on the seasonal pattern of ecosystem respiration in deciduous forests, *Glob. Chang. Biol.*, 21(1), 363–  
1033 376, doi:10.1111/gcb.12671, 2015.

1034 Mohanty, B. P., Cosh, M. H., Lakshmi, V. and Montzka, C.: Soil moisture remote sensing: State-of-the-science,  
1035 *Vadose Zo. J.*, doi:10.2136/vzj2016.10.0105, 2017.

1036 Mu, Q., Zhao, M. and Running, S. W.: MODIS Global Terrestrial Evapotranspiration (ET) Product  
1037 (MOD16A2/A3), Algorithm Theor. Basis Doc., 2013.

1038 NASA: Moderate Resolution Imaging Spectroradiometer ( MODIS ) Overview, Nasa, 2008.

1039 ~~Ng, G., Bedford, D. and Miller, D.: A mechanistic modeling and data assimilation framework for Mojave Desert  
1040 ecohydrology, *Water Resour. Res.*, 4662–4685, doi:10.1002/2014WR015281.Received, 2014.~~

1041 ~~Noormets, A., Desai, A. R., Cook, B. D., Euskirchen, E. S., Ricciato, D. M., Davis, K. J., Bolstad, P. V., Schmid, H.  
1042 P., Vogel, C. V., Carey, E. V., Su, H. B. and Chen, J.: Moisture sensitivity of ecosystem respiration: Comparison of  
1043 14 forest ecosystems in the Upper Great Lakes Region, USA, *Agric. For. Meteorol.*,  
1044 doi:10.1016/j.agrformet.2007.08.002, 2008.~~

1045 ~~Novick, K. A., Oishi, A. C., Ward, E. J., Siqueira, M. B. S., Juang, J. Y. and Stoy, P. C.: On the difference in the net  
1046 ecosystem exchange of CO2 between deciduous and evergreen forests in the southeastern United States, *Glob.  
1047 Chang. Biol.*, 21(2), doi:10.1111/gcb.12723, 2015.~~

1048 Olah, C.: Understanding LSTM Networks, <https://colah.github.io/posts/2015-08-Understanding-LSTMs/>, 2015,

1049 2015.

1050 Oleson, K. W., Lawrence, D. M., Bonan, G. B., Drewniak, B., Huang, M., Koven, C. D., Levis, S., Li, F., Riley, J.,  
1051 Subin, Z. M., Swenson, S. C., Thornton, P. E., Bozbiyik, A., Fisher, R. A., Heald, C. L., Kluzek, E., Lamarque, J.-  
1052 F., Lawrence, P. J., Leung, L. R., Lipscomb, W., Muszala, S., Ricciuto, D. M., Sacks, W. J., Sun, Y., Tang, J. and  
1053 Yang, Z.-L.: Technical Description of version 4.5 of the Community Land Model (CLM)., 2013.

1054 Omernik, J. M.: Perspectives on the nature and definition of ecological regions., *Environ. Manage.*,  
1055 doi:10.1007/s00267-003-5197-2, 2004.

1056 Omernik, J. M. and Griffith, G. E.: Ecoregions of the Conterminous United States: Evolution of a Hierarchical  
1057 Spatial Framework, *Environ. Manage.*, doi:10.1007/s00267-014-0364-1, 2014.

1058 Oyler, J. W., Dobrowski, S. Z., Ballantyne, A. P., Klene, A. E. and Running, S. W.: Artificial amplification of  
1059 warming trends across the mountains of the western United States, *Geophys. Res. Lett.*,  
1060 doi:10.1002/2014GL062803, 2015.

1061 Paca, V. H. da M., Espinoza-Dávalos, G. E., Hessels, T. M., Moreira, D. M., Comair, G. F. and Bastiaanssen, W. G.  
1062 M.: The spatial variability of actual evapotranspiration across the Amazon River Basin based on remote sensing  
1063 products validated with flux towers, *Ecol. Process.*, 8(1), doi:10.1186/s13717-019-0158-8, 2019.

1064 ~~Pedersen, S. H., Liston, G. E., Tamstorf, M. P., Abermann, J., Lund, M. and Schmidt, N. M.: Quantifying snow  
1065 controls on vegetation greenness, *Ecosphere*, doi:10.1002/ecs2.2309, 2018.~~

1066 ~~PRIESTLEY Priestley, C. H. B. and TAYLOR Taylor, R. J.: On the Assessment of Surface Heat Flux and  
1067 Evaporation Using Large-Scale Parameters, *Mon. Weather Rev.*, doi:10.1175/1520-  
1068 0493(1972)100<0081:otaosh>2.3.co;2, 1972.~~

1069 Pumpanen, J., Kolari, P., Ilvesniemi, H., Minkkinen, K., Vesala, T., Niinistö, S., Lohila, A., Larmola, T., Morero,  
1070 M., Pihlatie, M., Janssens, I., Yuste, J. C., Grünzweig, J. M., Reth, S., Subke, J. A., Savage, K., Kutsch, W.,  
1071 Østreng, G., Ziegler, W., Anthoni, P., Lindroth, A. and Hari, P.: Comparison of different chamber techniques for  
1072 measuring soil CO<sub>2</sub> efflux, *Agric. For. Meteorol.*, doi:10.1016/j.agrformet.2003.12.001, 2004.

1073 ~~Qiao, Z., Xu, X., Zhao, M., Wang, F. and Liu, L.: The application of a binary division procedure to the classification  
1074 of forest subcategories using MODIS time series data during 2000–2010 in China, *Int. J. Remote Sens.*,  
1075 doi:10.1080/01431161.2016.1176269, 2016.~~

1076 Reichstein, M., Falge, E., Baldocchi, D., Papale, D., Aubinet, M., Berbigier, P., Bernhofer, C., Buchmann, N.,  
1077 Gilmanov, T., Granier, A., Grünwald, T., Havránková, K., Ilvesniemi, H., Janous, D., Knohl, A., Laurila, T., Lohila,  
1078 A., Loustau, D., Matteucci, G., Meyers, T., Miglietta, F., Ourcival, J. M., Pumpanen, J., Rambal, S., Rotenberg, E.,  
1079 Sanz, M., Tenhunen, J., Seufert, G., Vaccari, F., Vesala, T., Yakir, D. and Valentini, R.: On the separation of net  
1080 ecosystem exchange into assimilation and ecosystem respiration: Review and improved algorithm, *Glob. Chang.*  
1081 *Biol.*, doi:10.1111/j.1365-2486.2005.001002.x, 2005.

1082 Reichstein, M., Camps-Valls, G., Stevens, B., Jung, M., Denzler, J., Carvalhais, N. and Prabhat: Deep learning and  
1083 process understanding for data-driven Earth system science, *Nature*, 566(7743), 195–204, doi:10.1038/s41586-019-  
1084 0912-1, 2019.

1085 Ren, H., Cromwell, E., Kravitz, B. and Chen, X.: Using Deep Learning to Fill Spatio-Temporal Data Gaps in  
1086 Hydrological Monitoring Networks, *Hydrol. Earth Syst. Sci. Discuss.*, (May), 1–20, doi:10.5194/hess-2019-196,  
1087 2019.

1088 Rungee, J., Bales, R. and Goulden, M.: Evapotranspiration response to multiyear dry periods in the semiarid western  
1089 United States, *Hydrol. Process.*, doi:10.1002/hyp.13322, 2019.

1090 Ryu, Y., Baldocchi, D. D., Kobayashi, H., Van Ingen, C., Li, J., Black, T. A., Beringer, J., Van Gorsel, E., Knohl,  
1091 A., Law, B. E. and Rouspard, O.: Integration of MODIS land and atmosphere products with a coupled-process  
1092 model to estimate gross primary productivity and evapotranspiration from 1 km to global scales, *Global*  
1093 *Biogeochem. Cycles*, 25(4), 1–24, doi:10.1029/2011GB004053, 2011.

1094 Seneviratne, S. I., Lüthi, D., Litschi, M. and Schär, C.: Land-atmosphere coupling and climate change in Europe,  
1095 Nature, doi:10.1038/nature05095, 2006.

1096 ~~Sloat, L. L., Henderson, A. N., Lamanna, C. and Enquist, B. J.: The Effect of the Foresummer Drought on Carbon  
1097 Exchange in Subalpine Meadows, Ecosystems, 18(3), 533–545, doi:10.1007/s10021-015-9845-1, 2015.~~

1098 Strachan, S., Kelsey, E. P., Brown, R. F., Dascalu, S., Harris, F., Kent, G., Lyles, B., McCurdy, G., Slater, D. and  
1099 Smith, K.: Filling the Data Gaps in Mountain Climate Observatories Through Advanced Technology, Refined  
1100 Instrument Siting, and a Focus on Gradients, Mt. Res. Dev., 36(4), 518–527, doi:10.1659/mrd-journal-d-16-00028.1,  
1101 2016.

1102 Suleau, M., Moureaux, C., Dufranne, D., Buysse, P., Bodson, B., Destain, J. P., Heinesch, B., Debacq, A. and  
1103 Aubinet, M.: Respiration of three Belgian crops: Partitioning of total ecosystem respiration in its heterotrophic,  
1104 above- and below-ground autotrophic components, Agric. For. Meteorol., doi:10.1016/j.agrformet.2011.01.012,  
1105 2011.

1106 Teuling, A. J., Van Loon, A. F., Seneviratne, S. I., Lehner, I., Aubinet, M., Heinesch, B., Bernhofer, C., Grünwald,  
1107 T., Prasse, H. and Spank, U.: Evapotranspiration amplifies European summer drought, Geophys. Res. Lett.,  
1108 doi:10.1002/grl.50495, 2013.

1109 Thornton, P. E., Thornton, M. M., Mayer, B. W., Wei, Y., Devarakonda, R., Vose, R. S. and Cook, R. B.: Daymet:  
1110 Daily Surface Weather Data on a 1-km Grid for North America, Version 3, ORNL DAAC, Oak Ridge, Tennessee,  
1111 USA, 2017.

1112 Tran, A. P., Rungee, J., Faybishenko, B., Dafflon, B. and Hubbard, S. S.: Assessment of spatiotemporal variability  
1113 of evapotranspiration and its governing factors in a mountainous watershed, Water (Switzerland), 11(2),  
1114 doi:10.3390/w11020243, 2019.

1115 U.S. Environmental Protection Agency: Level III Ecoregions of the Continental United States, Environ. Prot., 2003.

1116 ~~Visser, A., Thaw, M., Deinhard, A., Bibby, R., Safeeq, M., Conklin, M., Esser, B. and Van der Velde, Y.:  
1117 Cosmogenic Isotopes Unravel the Hydrochronology and Water Storage Dynamics of the Southern Sierra Critical  
1118 Zone, Water Resour. Res., doi:10.1029/2018WR023665, 2019.~~

1119 Viviroli, D. and Weingartner, R.: “Water towers”—A global view of the hydrological importance of mountains, in  
1120 Advances in Global Change Research., 2008.

1121 Viviroli, D., Dürr, H. H., Messlerli, B., Meybeck, M. and Weingartner, R.: Mountains of the world, water towers for  
1122 humanity: Typology, mapping, and global significance, Water Resour. Res., 43(7), 1–13,  
1123 doi:10.1029/2006WR005653, 2007.

1124 Vogelmann, J. E., Howard, S. M., Yang, L., Larson, C. R., Wylie, B. K. and Van Driel, N.: Completion of the 1990s  
1125 National Land Cover Data set for the conterminous United States from Landsat thematic mapper data and ancillary  
1126 data sources, Photogramm. Eng. Remote Sensing, 2001.

1127 ~~Wainwright, H. M., Steefel, C., Trutner, S. D., Henderson, A. N., Nikolopoulos, E. I., Wilmer, C. F., Chadwick, K.  
1128 D., Falco, N., Schaettle, K. B., Brown, J. B., Steltzer, H., Williams, K. H., Hubbard, S. and Enquist, B. J.: Satellite-  
1129 derived foresummer drought sensitivity of plant productivity in Rocky Mountain headwater catchments: spatial  
1130 heterogeneity and geological-geomorphological control, Environ. Res. Lett., doi:10.1088/1748-9326/ab8fd0, 2020.~~

1131 ~~Wang, B., Zha, T. S., Jia, X., Wu, B., Zhang, Y. Q. and Qin, S. G.: Soil moisture modifies the response of soil  
1132 respiration to temperature in a desert shrub ecosystem, Biogeosciences, 11(2), 259–268, doi:10.5194/bg-11-259-  
1133 2014, 2014.~~

1134 Webb, R. W., Fassnacht, S. R. and Gooseff, M. N.: Hydrologic flow path development varies by aspect during  
1135 spring snowmelt in complex subalpine terrain, Cryosphere, 12(1), 287–300, doi:10.5194/tc-12-287-2018, 2018.

1136 Wieder, W. R., Knowles, J. F., Blanken, P. D., Swenson, S. C. and Suding, K. N.: Ecosystem function in complex  
1137 mountain terrain: Combining models and long-term observations to advance process-based understanding, J.  
1138 Geophys. Res. Biogeosciences, doi:10.1002/2016JG003704, 2017.

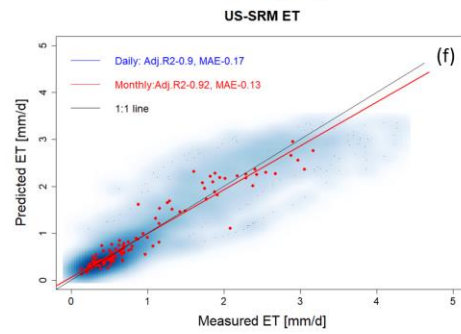
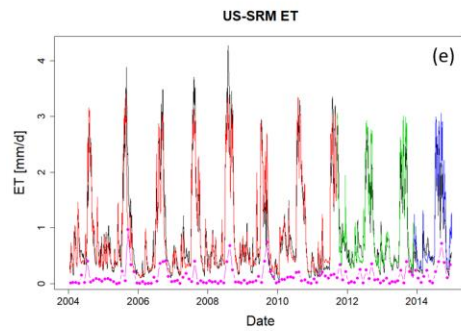
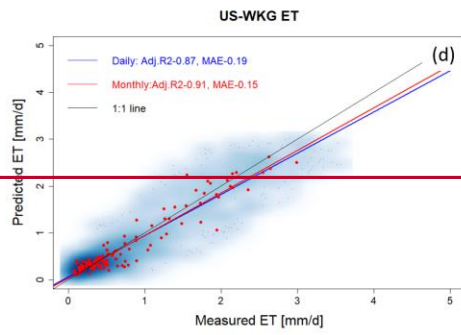
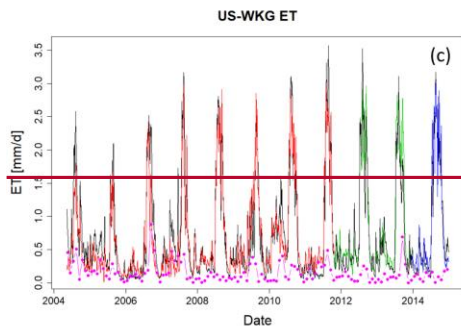
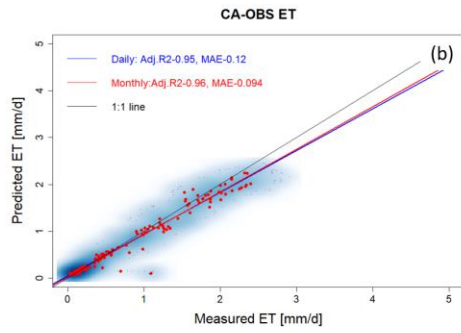
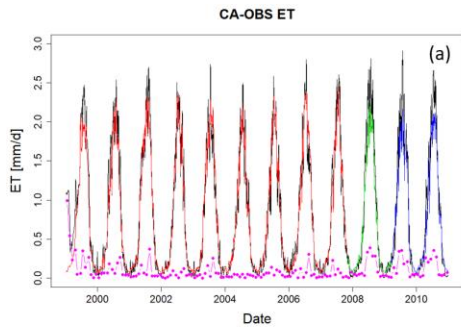
- 1139 Williams, C. A. and Albertson, J. D.: Soil moisture controls on canopy-scale water and carbon fluxes in an African  
1140 savanna, *Water Resour. Res.*, doi:10.1029/2004WR003208, 2004.
- 1141 Williams, M., Richardson, A. D., Reichstein, M., Stoy, P. C., Peylin, P., Verbeeck, H., Carvalhais, N., Jung, M.,  
1142 Hollinger, D. Y., Kattge, J., Leuning, R., Luo, Y., Tomelleri, E., Trudinger, C. and Wang, Y.-P.: Improving land  
1143 surface models with FLUXNET data, *Biogeosciences Discuss.*, doi:10.5194/bgd-6-2785-2009, 2009.
- 1144 Wilson, K. B., Hanson, P. J., Mulholland, P. J., Baldocchi, D. D. and Wullschleger, S. D.: A comparison of methods  
1145 for determining forest evapotranspiration and its components: Sap-flow, soil water budget, eddy covariance and  
1146 catchment water balance, *Agric. For. Meteorol.*, 106(2), 153–168, doi:10.1016/S0168-1923(00)00199-4, 2001.
- 1147 Xiao, J., Ollinger, S. V., Frolking, S., Hurtt, G. C., Hollinger, D. Y., Davis, K. J., Pan, Y., Zhang, X., Deng, F.,  
1148 Chen, J., Baldocchi, D. D., Law, B. E., Arain, M. A., Desai, A. R., Richardson, A. D., Sun, G., Amiro, B., Margolis,  
1149 H., Gu, L., Scott, R. L., Blanken, P. D. and Suyker, A. E.: Data-driven diagnostics of terrestrial carbon dynamics  
1150 over North America, *Agric. For. Meteorol.*, doi:10.1016/j.agrformet.2014.06.013, 2014.
- 1151 Xu, H., Xiao, J., Zhang, Z., Ollinger, S. V., Hollinger, D. Y., Pan, Y. and Wan, J.: Canopy photosynthetic capacity  
1152 drives contrasting age dynamics of resource use efficiencies between mature temperate evergreen and deciduous  
1153 forests, *Glob. Chang. Biol.*, 26(11), doi:10.1111/gcb.15312, 2020.
- 1154 Xu, L., Baldocchi, D. D. and Tang, J.: How soil moisture, rain pulses, and growth alter the response of ecosystem  
1155 respiration to temperature, *Global Biogeochem. Cycles*, 18(4), 1–10, doi:10.1029/2004GB002281, 2004.
- 1156 Xu, T., Guo, Z., Liu, S., He, X., Meng, Y., Xu, Z., Xia, Y., Xiao, J., Zhang, Y., Ma, Y. and Song, L.: Evaluating  
1157 Different Machine Learning Methods for Upscaling Evapotranspiration from Flux Towers to the Regional Scale, *J.*  
1158 *Geophys. Res. Atmos.*, 123(16), 8674–8690, doi:10.1029/2018JD028447, 2018.
- 1159 Zhang, L., Potter, N., Hickel, K., Zhang, Y. and Shao, Q.: Water balance modeling over variable time scales based  
1160 on the Budyko framework - Model development and testing, *J. Hydrol.*, 360(1–4), 117–131,  
1161 doi:10.1016/j.jhydrol.2008.07.021, 2008.
- 1162 Zhang, Y., Kong, D., Gan, R., Chiew, F. H. S., McVicar, T. R., Zhang, Q. and Yang, Y.: Coupled estimation of  
1163 500 m and 8-day resolution global evapotranspiration and gross primary production in 2002–2017, *Remote Sens.*  
1164 *Environ.*, 222(May 2018), 165–182, doi:10.1016/j.rse.2018.12.031, 2019.

1165

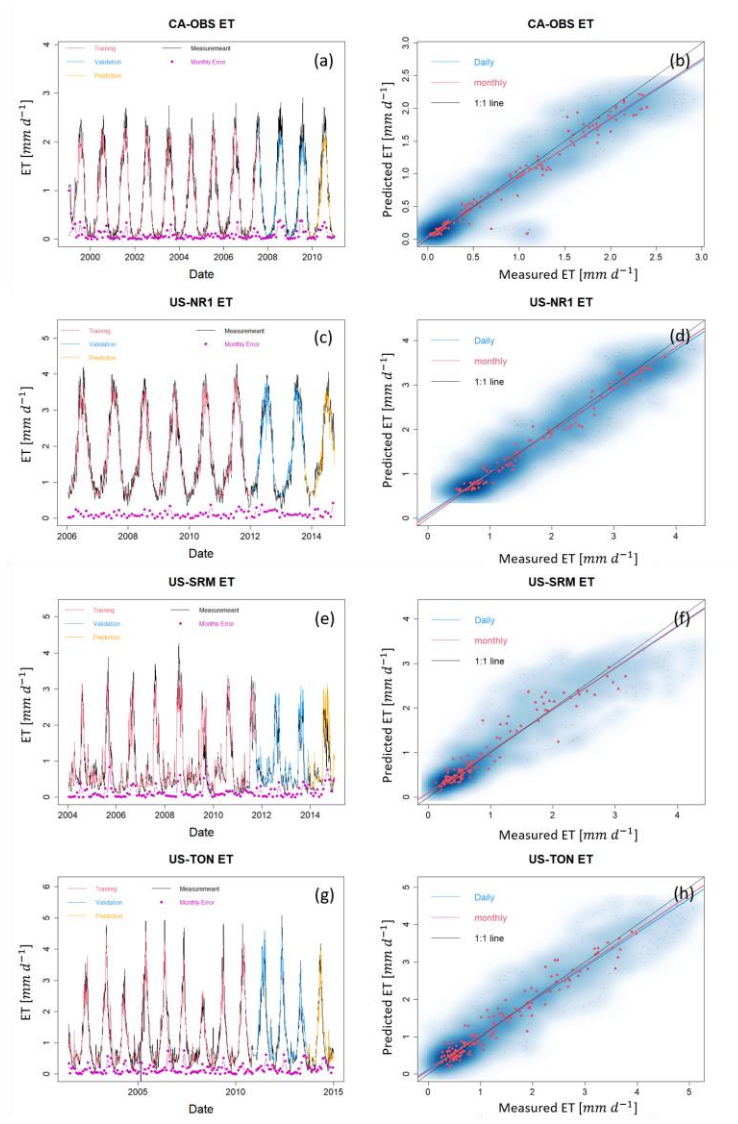
## 1166 Appendix

1167

### 1168 1. ET and $R_{ECO}$ Estimation over Time at other Fluxnet sites



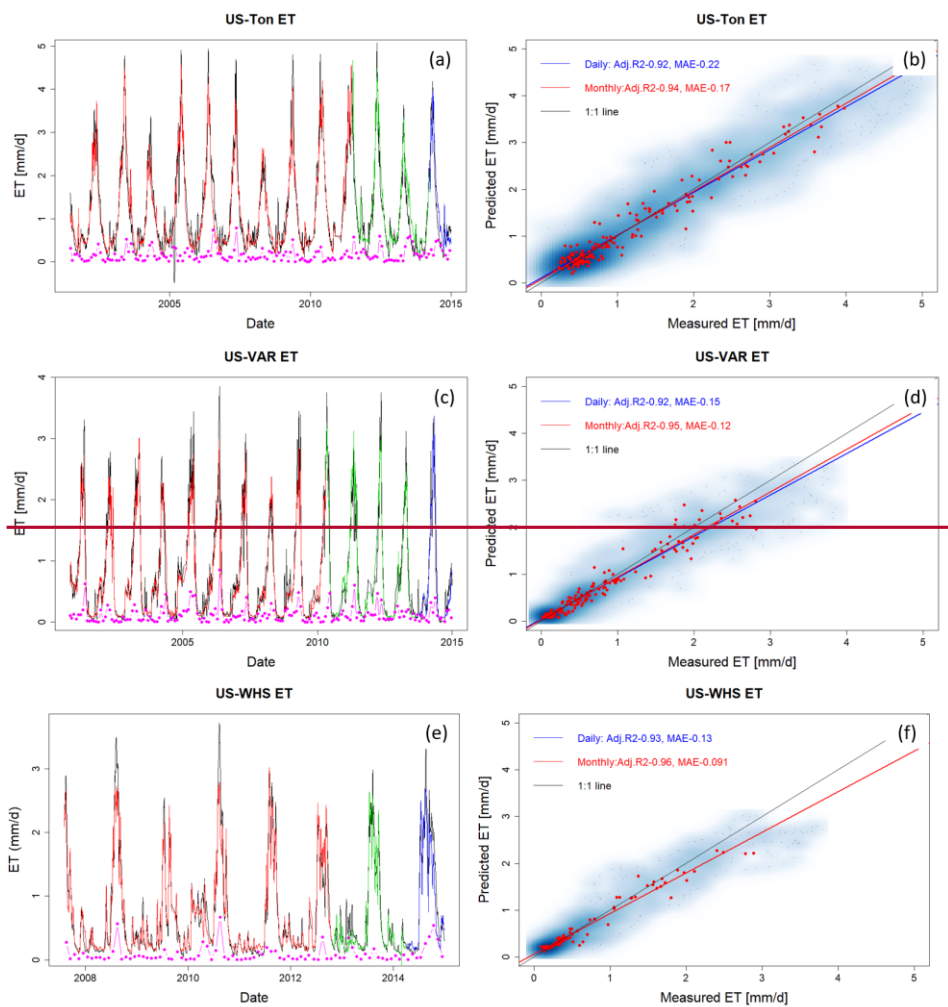




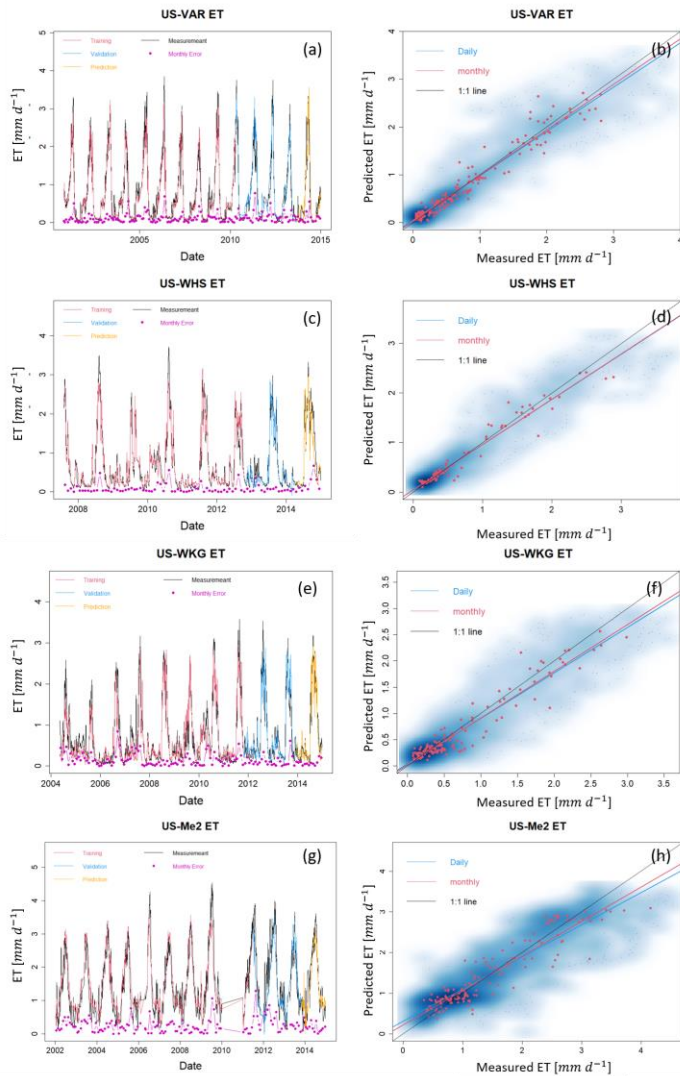
1170  
 1171 **Figure A1: ET estimation with data from selected FLUXNET sites at CA-OBS, US-NR1, US-SRM, and US-TON.**  
 1172 **Panels (a), (c), (e) and (g) present daily estimations of ET with red, green, and blue lines representing data used separated**  
 1173 **for training, validation, and prediction, respectively, and the black line representing the eddy covariance measurement.,**  
 1174 **Pink points describe depict monthly mean difference error between HPM estimation and measured FLUXNET data. Panels**

1175 (b), (d), (f) and (h) show the scatter plots of daily (blue) and monthly (red) ET. Darker blue clouds represent greater density  
1176 of data points.

1177



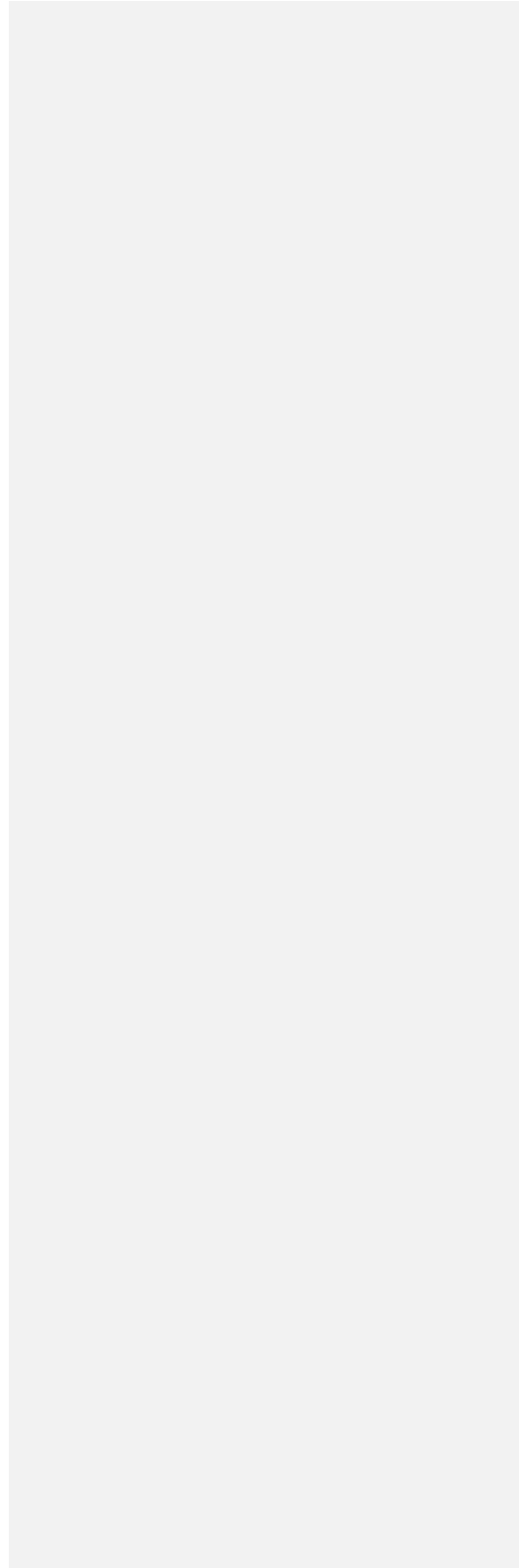
1178

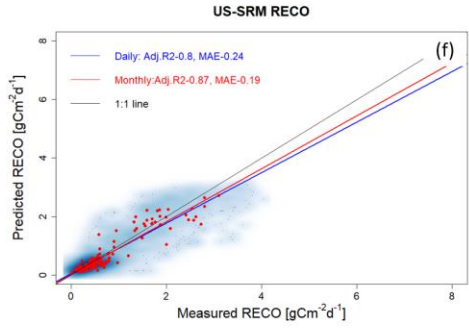
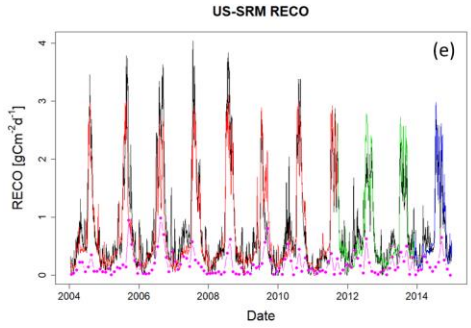
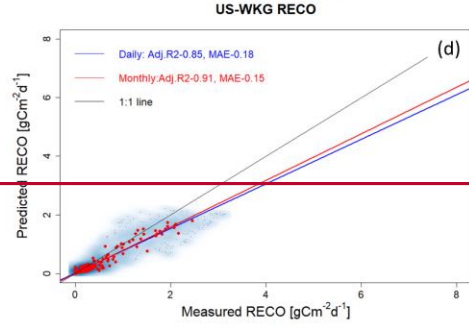
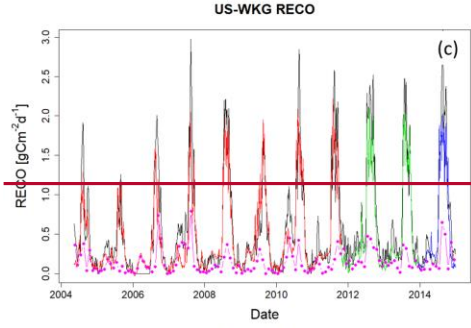
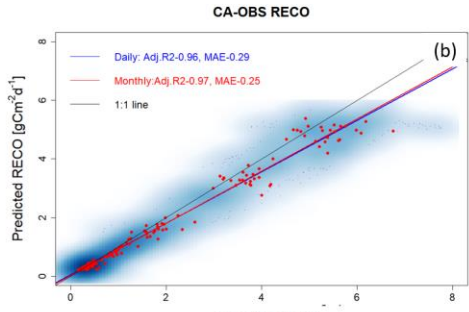
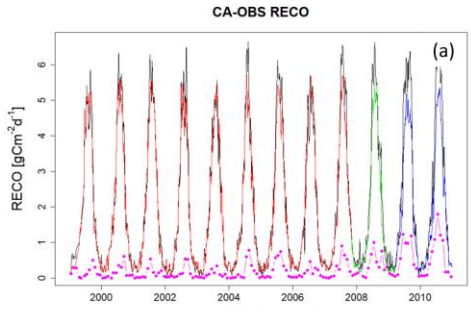


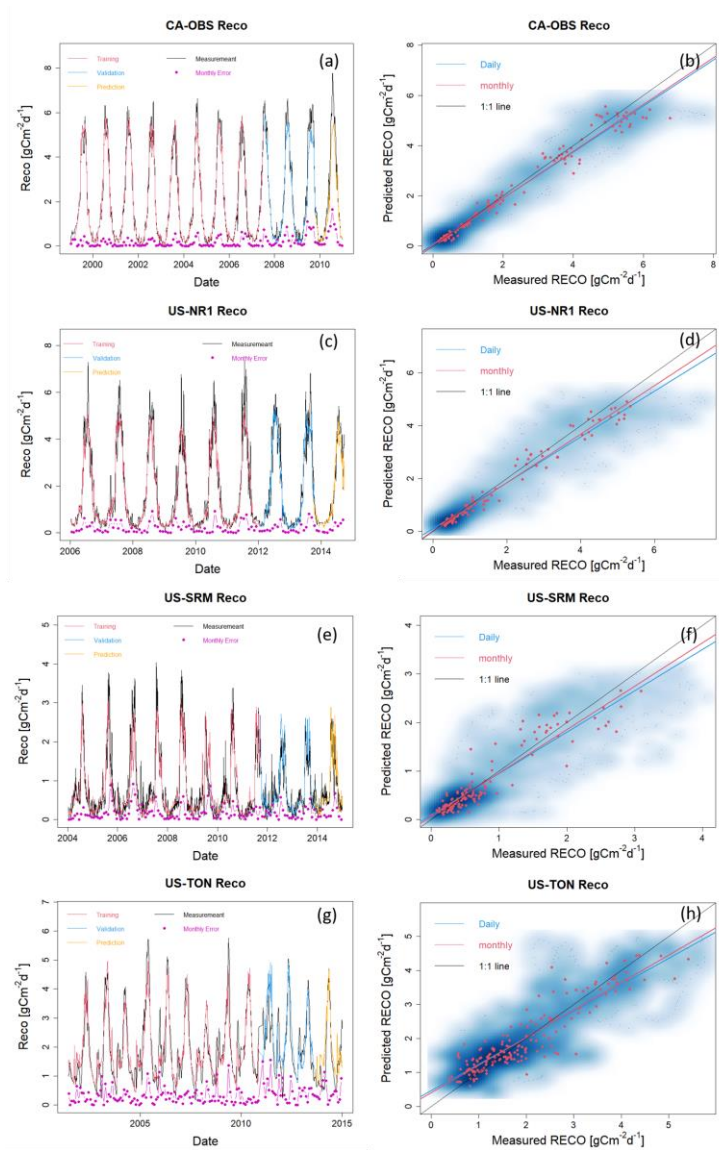
1179  
 1180 **Figure A2: ET estimation with data from selected FLUXNET sites at US-Ton, US-Var, and US-Whs-, US-Wkg and US-**  
 1181 **Me2. Panels (a), (c), and (e) and (g) present daily estimations of ET with red, green, and blue lines representing data**  
 1182 **used separated for training, validation, and prediction, respectively, and the black line representing the eddy covariance**  
 1183 **measurement. Pink points described depict monthly mean difference error between HPM estimation and**  
 1184 **measured FLUXNET data. Panels (b), (d), (f) and (h) show the scatter plots of daily (blue) and monthly (red) ET. Darker**  
 1185 **blue clouds represent greater density of data points.**

1186

1187



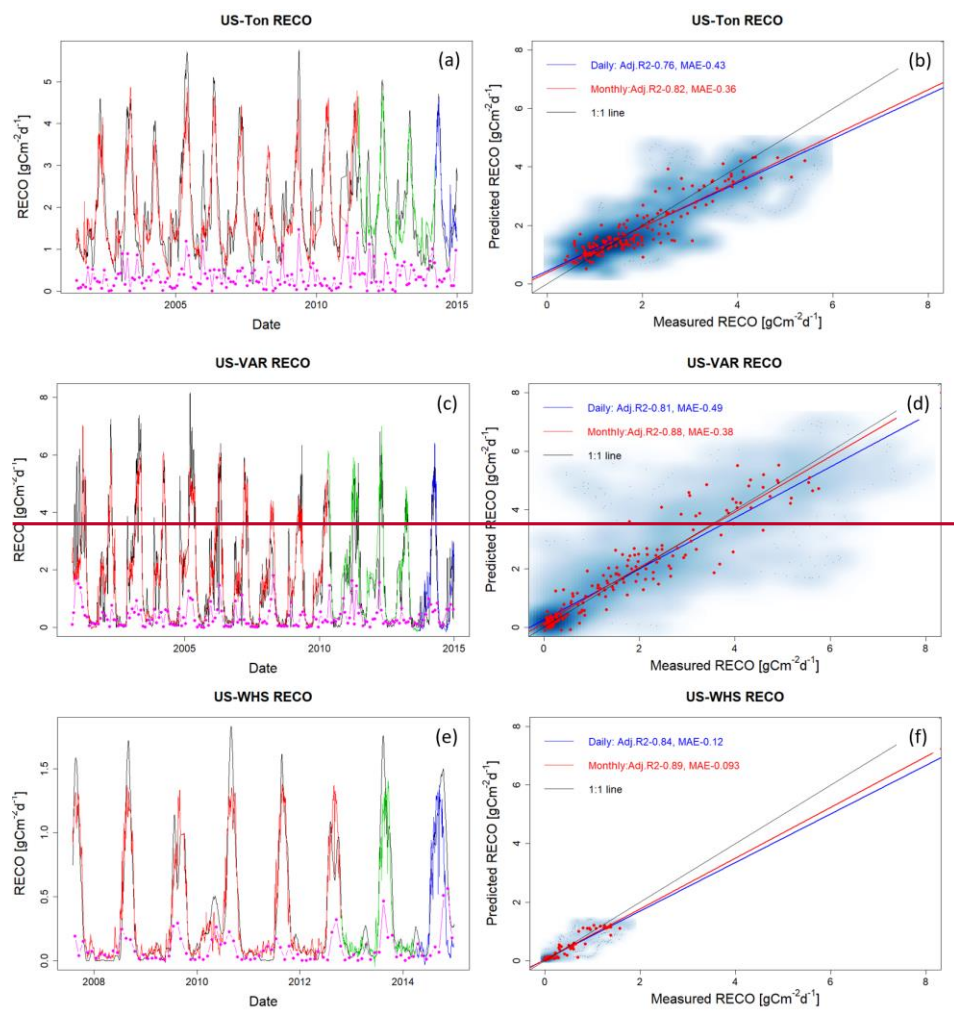




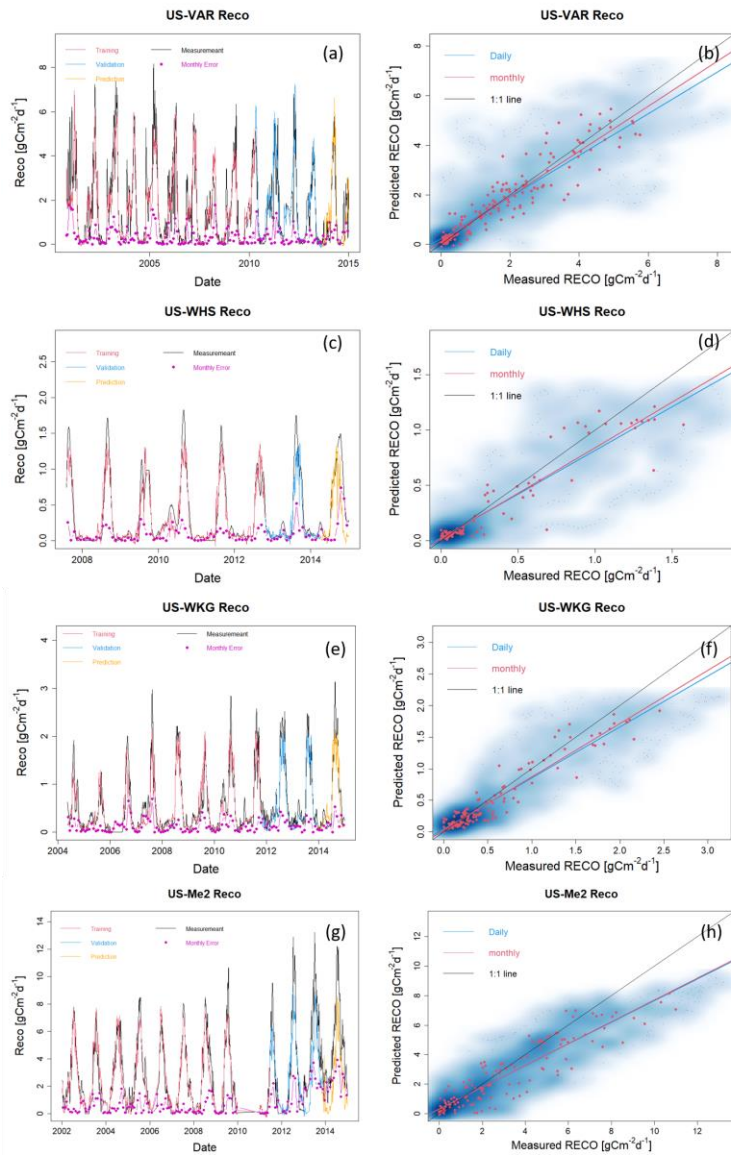
1189  
 1190 Figure A3:  $R_{eco}$  estimation with data from selected FLUXNET sites at CA-OBS, US-NR1, US-SRM, and US-  
 1191 SRM-Ton. Panels (a), (c), (e) and (g) present daily estimations of  $R_{eco}$  with red, green, and blue lines representing data  
 1192 used for training, validation, and prediction, respectively, and the black line is eddy covariance measurement.  
 1193 Pink points describe the monthly mean difference between HPM estimation and measured FLUXNET data.

1194 Panels (b), (d), and (f) show the scatter plots of daily (blue) and monthly (red)  $R_{\text{RECO}}$  vs  $R_{\text{CO}_2}$ . Darker blue clouds  
1195 represent greater density of data points.

1196



1197

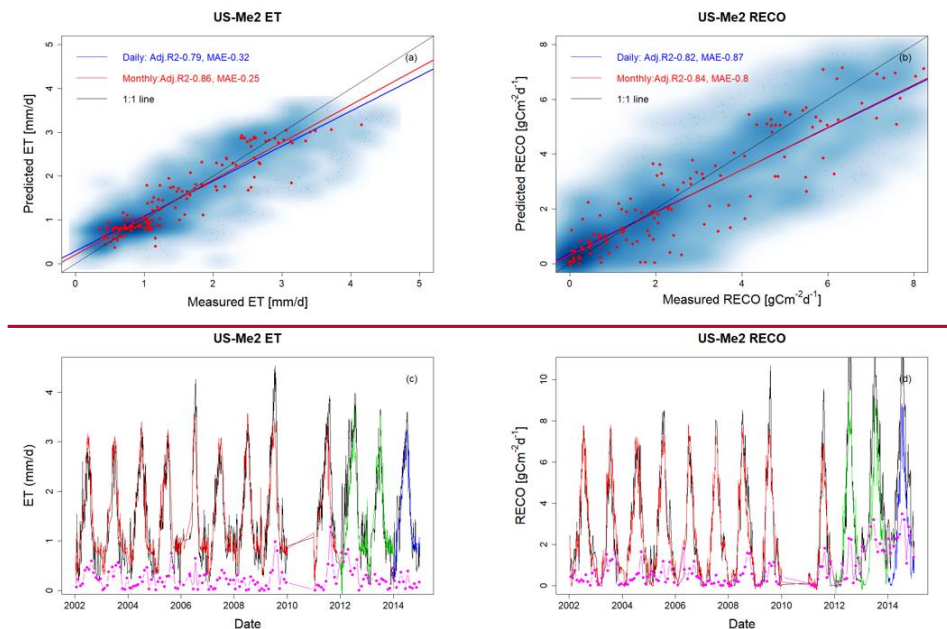


1198  
 1199 **Figure A4:**  $R_{ECO}$  estimation with data from selected FLUXNET sites at US-Ton, US-Var, and US-Whs, US-Wkg and  
 1200 **US-Me2.** Panels (a), (c), and (e) and (g) present daily estimations of  $R_{ECO}$  with red, green, and blue lines representing data  
 1201 used  $R_{ECO}$  separated for training, validation, and prediction, respectively, and the black line representing the eddy covariance  
 1202 measurement. Pink points describe depict monthly mean-difference error between HPM estimation and

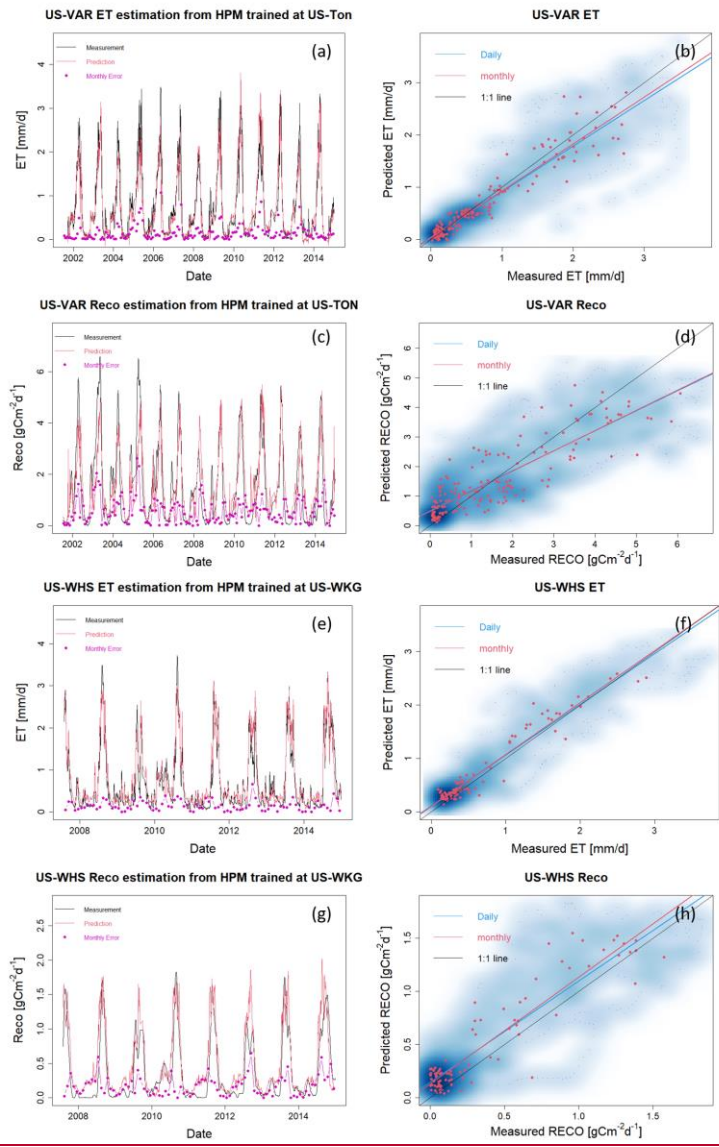


1203 measured FLUXNET data. Panels (b), (d), and (f) and (h) show the scatter plots of daily (blue) and monthly (red)  $R_{ETQ}$ - $R_{ECO}$ .  
 1204 Darker blue clouds represent greater density of data points.

1205  
 1206



1207  
 1208 **Figure A5: ET and  $R_{ETQ}$  estimation at US-Me2. Panels (a) and (b) show the scatter plots of daily (blue) and monthly (red)**  
 1209 **ET and  $R_{ETQ}$ . Darker blue clouds represent greater density of data points. Panels (c), and (d) present daily estimations of**  
 1210  **$R_{ETQ}$  with red, green, and blue lines representing data used for training, validation, and prediction, respectively, and the**  
 1211 **black line representing the eddy covariance measurement. Pink points describe monthly mean difference between HPM**  
 1212 **estimation and measured data.**



1213

1214

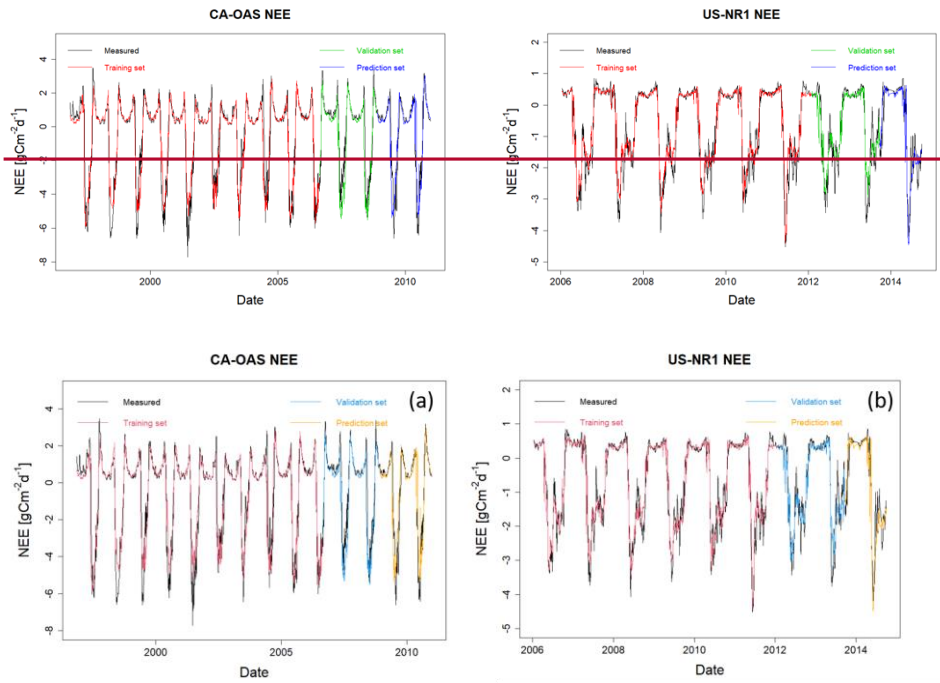
1215 Figure A5: Use case 2. ET and Reco estimation at US-Var and US-Whs from HPM trained at US-Ton and US-Wky,

1216 respectively.

1217

1218 **2. Tested NEE Estimation over Time at CA-OAS and US-NR1**

1219



1220

1221 **Figure A6. HPM estimate of NEE at CA-OAS and US-NR1.  $R^2$  between estimation and measurements are 0.87, 0.83 and**  
1222 **0.81 at CA-OAS; 0.94, 0.88 and 0.90 at US-NR1 for the training set, validation set and prediction set, respectively. Model**  
1223 **inputs include air temperature, soil temperature, sn, precipitation and radiation.**

1224

1225

Formatted: Line spacing: Multiple 1.08 li